This is the peer-reviewed, final accepted version for American Mineralogist, published by the Mineralogical Society of America.
The published version is subject to change. Cite as Authors (Year) Title. American Mineralogist, in press.
DOI: https://doi.org/10.2138/am-2022-8007. http://www.minsocam.org/

**Revision 3**

# Carbon flux and alkaline volcanism: evidence from carbonatite-like carbonate minerals in trachytes, Ulleung Island, South Korea

ShuangShuang Chen[a, b], Minghua Ren[c*], Hyejeong Lee[c], Eugene Smith[c], Shichun Huang[c], Seung Gu Lee[d], TaeJong Lee[d], Rui Gao[a, b]

[a] *School of Earth Sciences and Engineering, Sun Yat-sen University, Guangzhou 510275, China*

[b] *Southern Marine Science and Engineering Guangdong Laboratory (Zhuhai), Zhuhai 519080, China*

[c] *Department of Geoscience, University of Nevada, Las Vegas, NV 89154, United States*

[d] *Geology Division, Korea Institute of Geoscience and Mineral Resources, 124 Gwahak-ro Yuseong-gu, Daejeon 34132, South Korea*

*Corresponding author.

Department of Geoscience, University of Nevada, Las Vegas, NV 89154, United States

E-mail address: minghua.ren@unlv.edu

This manuscript contains 8427 words, 8 figures, 5 tables, and 2 supplements

# Abstract

Carbon flux metasomatism in the subduction environment is an important process, but it remains poorly understood. The paucity of exposed lower crust and upper mantle rocks in continental arcs renders xenoliths a major target for studying the slab-derived carbon cycle. This study of the carbonate phases in volcanic rocks from three drill cores in Ulleung Island, South Korea, sheds light on the interaction of carbon flux in the upper mantle and lower crust in a back-arc setting. The volcanic rocks from Ulleung Island range in composition from trachybasalt to trachyte and contain abundant euhedral pseudomorphic carbonate grains, ulvöspinel-hosted and biotite-hosted carbonate-silicate melt inclusions, and irregular carbonate globules. Integrated petrographic and geochemical studies of a variety of phenocrysts, carbonate phases, and carbonate-silicate inclusions in biotite and ulvöspinel indicate that recharging of carbon flux affected magma evolution. Carbon and oxygen isotopes of the pseudomorphic carbonate grains overlap with mantle values, indicating a carbonatite-like origin of the carbonate phases. The (MgO, FeO, CaO)-rich silicates in ulvöspinel-hosted silicate inclusions and pseudomorphic carbonate grains likely represent a primary melt, which formed from partial melting of carbonated eclogite of the subducted slab within the mantle wedge beneath Ulleung Island. A petrogenetic model is proposed to illustrate that the crystal mush in the magma chamber was intruded by carbonate-rich liquids and caused alteration of cumulate crystals to generate the euhedral pseudomorphic carbonate grains. The extrusive magma captured those pseudomorphic grains and erupted to form the trachybasalt-trachyte units. The observed carbonate phases and their geochemical characteristics indicate that carbon flux metasomatism played a fundamental role in this back-arc magmatism.


**Keywords:** euhedral pseudomorphic carbonate grains; carbonate-silicate melt inclusion; carbon flux; trachytic magma; Ulleung Island

This is the peer-reviewed, final accepted version for American Mineralogist, published by the Mineralogical Society of America.
The published version is subject to change. Cite as Authors (Year) Title. American Mineralogist, in press.
DOI: https://doi.org/10.2138/am-2022-8007. http://www.minsocam.org/

## 1. Introduction

Carbonate metasomatism is common in subduction zones (e.g. Yaxley et al., 1991; Dasgupta and Hirschmann, 2010; Johnston et al., 2011; Mason et al., 2017). The studies of the geochemical character of back-arc volcanism increased the understanding of the origin and evolution of supercritical fluids in subduction zones (Hack et al., 2007; Frezzotti and Ferrando, 2015; Zhang et al., 2017). As a part of the volatile components, $CO_2$ emission from volcanoes is an important part of the global carbon cycle (Burton et al., 2013; Kelemen and Manning, 2015; Creon et al., 2017). Carbon flux is an important agent in mantle metasomatism that contributes to mantle geochemical heterogeneity (Tilton and Kwon, 1990; Dasgupta et al., 2009; Whitlet et al., 2019). Even though some subducted carbonates break down in the subduction zone and are released through arc volcanism, most of the subducted carbon can be transported into deeper mantle (e.g. Bebout, 1996; Jarrard, 2003; Frezzotti et al., 2011; Whitlet et al., 2019). The predicted global slab-derived carbon flux escaping from the subducted crust at the subarc region records only a portion of the carbon cycle (Kerrick and Connolly, 2001; Jarrard, 2003; Gorman et al., 2006; Bebout and Penniston-Dorland, 2016; Whitlet et al., 2019) and a large amount of carbon should be preserved in the mantle and crust due to metasomatism (Yaxley et al., 1991; Bebout, 1996, 2007; Marty and Tolstikhin, 1998).

Carbonatite is important for studying the long-term deep carbon cycle within the Earth (Dasgupta and Hirschmann, 2010, Frezzotti et al., 2011; Hermann et al., 2013). Based on current studies, the influence of carbon flux on the formation of alkaline silicate rocks is highly speculative and the relationship between them has been controversial (Kogarko et al., 2001; Laporte et al., 2014; Zhang et al., 2017; Loges et al., 2019). Some alkaline silicate melts and their fractionation series can be closely linked to carbonate metasomatism (Yaxley et al., 1991; Kogarko et al., 2001; Hoernle et al., 2002; Brandl et al., 2015) and many alkaline silicate rocks are directly associated with carbonatites (Harmer, 1999; Hoernle et al., 2002; Le Bas, 2008; Jones et al., 2013; Brandl et al., 2015; Weidendorfer et al., 2016). The most direct observations of carbonatite in the mantle are from melt pockets hosted in xenoliths (Coltorti et al., 1999; Neumann et al., 2002; Fulignati et al., 2001; Hudgins et al., 2015; Creon et al., 2017; Loges et al., 2019) and inclusions in diamonds (Navon et al., 1988; Schrauder and Navon 1994; Frezzotti et al., 2011; Weiss et al., 2015). The carbonate-metasomatized xenoliths in the alkali basalts from oceanic islands record the carbonatite melt infiltration in mantle peridotite (Coltorti et al., 1999;

Kogarko et al., 2001; Neumann et al., 2002; Moine et al., 2004). Experimental work shows that both hydrous and carbonate fluids can be generated from carbonate metasomatized amphibole-peridotite and the two fluids can easily mix to form carbon flux because of their low viscosity and high mobility (Schrauder and Navon, 1994; Poli et al., 2009). The growing number of studies of carbonatites from oceanic islands and deep subduction zones have greatly increased our knowledge of the carbon cycle within the Earth system (Coltorti et al., 1999; Moine et al., 2004; Walter et al., 2008; Jones et al., 2013; Li et al., 2020).

Even though there are numerous reports of carbonate-metasomatized mantle xenoliths (Pyle and Haggerty, 1994; Hammouda, 2003; Frezzotti et al., 2011; Weiss et al., 2015) and estimates of carbon flux from subduction zones (Jarrard, 2003; Burton et al., 2013; Dasgupta, 2013; Kelemen and Manning, 2015; Creon et al., 2017), the mechanisms and magnitudes of carbon transfer from the mantle to the surface remain vague. The opportunity to directly obtain deep subcrustal samples is rare. A few deep drilling projects have reached the gabbro layers of the oceanic crust, which were unroofed by faults (Alt and Teagle, 1999). These gabbros contain a higher amount of carbon than regular gabbros (Bach et al., 2001; Moine et al., 2004). To date, direct evidence of carbon activity in the subarc region is sparse. In core samples of this study, different types of carbonate minerals are preserved as mineral grains and inclusions. As such, the petrographic and geochemical signatures of these carbonate phases in the Ulleung Island volcanic rocks can shed light on carbonate-metasomatism within the back-arc crust.

This study investigated drill cores obtained from exploration drilling for geothermal investigations at Ulleung Island. The rocks include a series of trachybasalt to trachyte, and are similar to the rocks exposed on the surface. The surface-exposed tephriphonolite and phonolite are believed to represent the fractional crystallization products of basaltic magma in the upper mantle and shallow subvolcanic reservoirs (Brenna et al., 2014; Chen et al., 2018). Different types of carbonate phases, such as, euhedral carbonate grains, ulvöspinel-hosted and biotite-hosted carbonate-silicate inclusions (some with the hexagonal shape), and spherical or irregular carbonate globules, which were not reported in previous work (Brenna et al., 2014; Chen et al., 2018; Choi, 2020), are observed in the drill core samples. Understanding how these carbonate phases formed is the main goal of this work. Micro-textures and chemical analyses of different types of carbonate grains and melt inclusions were performed by using petrographic microscopy, scanning electron microscopy coupled with energy dispersive X-ray spectroscopic analysis,

112 electron microprobe analysis, and C-O isotopic studies. The majority of carbonate minerals are
113 Fe-Mg-Ca carbonate, which is classified as ankerite based on chemical composition. This study
114 has two objectives: (1) understanding the formation of carbonate minerals within this volcanic
115 suite, including the euhedral ankerite, hexagonal inclusions of coexisting carbonate-silicate
116 phases in biotite, and the anhedral sub-rounded ankerite in the matrix; and (2) evaluating the
117 effect of carbon flux and carbonate metasomatism in the formation of alkali silicate melts at
118 Ulleung Island.
119
120 **2. Geological setting, sampling site, and analytical methods**
121 **2.1 Ulleung Island volcanic rocks and the selected research targets**
122 Ulleung Island is one of the Late Cenozoic subaerial and submarine volcanoes in the
123 northern Ulleung Basin (37°30′N, 130°52′E), located in the southwestern part of the East Sea off
124 the eastern coast of the Korean Peninsula (Fig. 1a). Ulleung Island formed by explosive
125 eruptions from Pleistocene (~1.4 Ma) to mid-Holocene (~5 ka B.P.), and the composite
126 stratovolcano erupted alkaline lavas and pyroclastic rocks, ranging from alkali basalt,
127 trachybasalt, trachyte/phonolite to pantellerite (Fig. 1b;) (Arai et al., 1981; Kim and Lee, 1983;
128 Xu et al., 1998; Kim et al., 1999; Park et al., 2007; Lee et al., 2011; Brenna et al., 2014; Lim et
129 al., 2014).
130 The Korean geothermal investigating project drilled at four locations in the east (GH-1),
131 west (GH-2), south (GH-3), and north (GH-4) sections of Ulleung Island (Fig. 1b). Detailed
132 sampling depths and lithological descriptions are presented in Figure 1c and Table 1. Based on
133 the rock lithology and mineralogy, we correlated units between the cores and divided the strata
134 into five sections (S1 to S5 from top to bottom) (Fig. 1c and Supplement I). Section 1 contains
135 trachyte and trachyandesite with phenocrysts of Na-rich plagioclase and biotite. Euhedral
136 carbonate grains occur in trachyandesite. Section 2 rocks are mainly trachyte containing alkali
137 feldspar phenocrysts. The euhedral carbonate grains are less abundant (Table 1). Section 3 rocks
138 are obsidians with plagioclase phenocrysts and calcite-filling vesicles. Section 4 rocks are
139 basaltic trachyandesite with plagioclase and sanidine phenocrysts. Section 5 contains
140 trachybasalt with clinopyroxene, plagioclase, and pseudomorphic euhedral grain filled with
141 colloform siderite and calcite. The colloform carbonate has calcite in the core and siderite in the
142 rim (Supplement I) and indicates a volatile-rich character. More detailed geochemical work is

143 needed to justify the formation of these pseudomorphic carbonate-filled grains and is beyond the
144 scope of this study.
145 This investigation focuses on the mineralogical characteristics of the trachyte and
146 trachyandesite in sections 1 and 2. Based on the mineralogical characteristics in the rock, a
147 petrological model is developed to explain the effects of carbon flux on the evolution of alkali
148 silicate magmatism on this island and its possible application to the entire back-arc region.
149
150 **2.2 Analytical methods**
151 Mineral analyses were performed using an electron probe microanalyzer (EPMA) with four
152 wavelength-dispersive spectrometers (WDS) by JEOL JXA-8900 at the Department of
153 Geoscience, University of Nevada Las Vegas (UNLV), and JEOL JXA-8230 at Shandong Bureau
154 of China Metallurgical Geology Bureau in Jinan. Based on the type of minerals, the operating
155 conditions were 15 kV accelerating voltage, 10 to 20 nA probe current, and 2 to 10 microns beam
156 diameter. A series of natural and synthetic standards were utilized based on the elemental
157 characters of each standard. Quantitative chemical analyses, x-ray maps, and backscattered
158 electron (BSE) images were collected for minerals and their inclusions.
159 Carbon and oxygen isotope compositions ($\delta^{13}C_{VPDB}$ and $\delta^{18}O_{SMOW}$) were analyzed in the Las
160 Vegas Isotope Science Laboratory (LVIS) at UNLV. In Ulleung drill-core samples, carbonates
161 typically show a slightly brownish tone compared to feldspars. Carbonate powders were
162 collected by mini-drilling of 15 euhedral pseudomorphic carbonate grains from four rock chips
163 in sections 116.00 to 116.91. Some powders were checked with SEM/EDS to confirm that the
164 carbonate was collected by drilling. 100–300 μg powders were loaded and reacted with
165 orthophosphoric acid for 10 minutes at 70°C in a Kiel IV carbonate device connected to a
166 Finnigan Delta V Plus mass spectrometer via dual-inlet. Carbon and oxygen isotopic results are
167 reported using δ notation, which measures per mil (‰) deviations from Vienna Pee Dee
168 Belemnite (VPDB). $\delta^{18}O_{VPDB}$ is then converted to Standard Mean Ocean Water (SMOW)
169 reference using $\delta^{18}O_{SMOW} = 1.03092 \times \delta^{18}O_{VPDB} + 30.92$ (Kim et al., 2015). Data were obtained
170 for 14 out of the 15 powders. The largest sample (around 350 μg) generated too much gas for the
171 Delta V Plus mass spectrometer and yielded no data. Analytical reproducibility was better than
172 0.1‰ (95% confidence) for both $\delta^{13}C$ and $\delta^{18}O$ values, which are estimated by repeat
173 measurements of USC-1 standard ($\delta^{13}C$ = 2.09‰; $\delta^{18}O_{VPDB}$ = −2.08‰) against limestone

174 standard NBS-19 ($\delta^{13}C$ = 1.95‰; $\delta^{18}O_{VPDB}$ = −2.21‰).

175

176 **3. Results**

177 **3.1. Petrography and mineral chemistry overview**

178 Ulleung Island trachyandesite and trachyte display a porphyritic texture (Table 1) and
179 contain plagioclase (10 vol.%) and biotite (15 vol.%) phenocrysts, euhedral carbonate grains (15
180 vol.%), apatite and Fe-oxides micro-phenocrysts, and groundmass (60 vol.%) with micron-size
181 tabular albite and sanidine (Figs. 2 to 4). Carbonate grains exist as individual grains and clusters
182 in the trachytic matrix. Abundant apatite and ulvöspinel coexist with biotite, plagioclase, and
183 pseudomorphic carbonate grains in the clusters (Figs, 2a-b, 3a). The groundmass is composed of
184 fine-grained tabular feldspars with trachytic texture (Fig. 2a). The representative mineral
185 compositions are listed in Tables 2-4.

186 The cross-sections of carbonate grains usually show prismatic and tabular crystal shapes
187 with six or eight edges (Fig. 2). Some carbonate grains have unique pseudomorph shapes (Figs.
188 2a-c, 2f-g), and some appear as multiple pseudomorph clusters (Figs. 2d, e, h). The shapes of
189 carbonate grains are identical to the crystal habits of pyroxene/amphibole, and are hence referred
190 "pseudomorphic carbonate grains". Based on EPMA data (Table 4, Supplement II), the carbonate
191 phases record varying ratios of Ca-Mg-Fe. Most carbonate phases have FeO ~15 wt.%, MgO ~10
192 wt.%, CaO ~ 30 wt.%, and are classified as ankerite (Fig. 5a). According to the varying Mg/Fe
193 ratios, ankerite may be described as Mg-rich or Fe-rich varieties. Within carbonate grains,
194 rhombic Mg-rich ankerite crystals are distributed within amorphous Fe-rich ankerite (Figs. 2f, g).
195 Some carbonate grains contain zoned Mg-rich ankerite in the center (Fig. 2h), which suggests the
196 Liesegang phenomena of periodic precipitation (Frezzotti and Ferrando, 2015). The carbonate
197 grains usually contain subhedral-euhedral apatite and ulvöspinel microcrystals. Biotite truncates
198 the euhedral ankerite grains (Figs. 2a, b). Euhedral-subhedral rod and needle-shaped apatite and
199 subhedral cubic shaped Fe-oxides coexist with biotite, plagioclase, and pseudomorphic ankerite
200 in clusters (Figs. 2a, d-f, 3a). Trachytic matrix corrodes and cuts the carbonate grains along the
201 cracks (Fig. 2e, f). Pseudomorphic ankerite grains are mainly found in sections 1 and 2. In
202 addition to their presence in mineral clusters and as individual grains, carbonate phases can also
203 exist as spherical and irregular globules in groundmass and inclusions in biotite and Fe-oxide
204 (Fig. 3a-c).

Biotite shows slight alteration along cleavages and contains a large number of inclusions, including euhedral to subhedral apatite, ilmenite (Figs. 3a, b), pseudomorphic carbonate grains (Fig. 3b), hexagonal shape inclusions (Figs. 3c, e, g, i) and irregular carbonate-silicate inclusions (Figs. 3f, h, j). Apatite and ulvöspinel coexist with ankerite in the hexagonal inclusions (Figs. 3d, f). Some carbonate inclusions show distinct zoning textures with increasing Mg content from edge to core (Fig. 3e). The inclusions with coexisting carbonate-silicate usually have a carbonate core and a silicate rim (Fig. 3d-j). The silicate rim is usually 1 to 2 micrometers wide and its petrographic character is difficult to identify. It shows amorphous behavior under cross-polarized light, but in most conditions, its optic character is affected by the surrounding minerals. Petrographic observation indicates a glassy silicate rim. Some inclusions in biotite consist of complex mineral assemblages with tablet-shaped feldspars, apatite, Fe-oxide, ankerite, and the relicts of silicate glass (Fig. 3f). Ankerite may be interstitially distributed between biotite crystals in the biotite-ankerite clusters (Fig. 4a), and silicate glasses form at the contact between carbonate and biotite (Figs. 3c-j, 4a). Some pseudomorphic or rounded silicate glass grains occur in the groundmass (Fig. 4b). The range of Mg-Fe content for the biotite is consistent with magnesio-biotite (Fig. 5b). Biotite has $TiO_2$ of 6.8-9.8 wt.% and BaO of 1-1.5 wt.%.

Feldspar phenocrysts occur as euhedral to subhedral grains and clusters (Figs. 4c-f). Most plagioclase phenocrysts have a sericite core and a rim that contains intergrown albite and ankerite (Fig. 4e, f). There is a thin coating of albite that mantles the pseudomorph feldspar. The plagioclase relicts have compositions of labradorite to bytownite (An 56-89) (Fig. 5c). In some rocks, the feldspar phenocrysts are anorthoclase (Ab 50-90, Or 7-47) with no alteration. The groundmass feldspars are unaltered albite, sanidine, and anorthoclase.

Apatite and aluminum-rich Fe-Ti oxide are the most common accessory phases (Table 2). They are abundant in the phenocryst clusters (Figs 2a, 3a). Subhedral to euhedral apatite of variable size (50-500 μm) are included in biotite, ankerite, silicate glass, and exist in the groundmass (Figs. 2-4). Apatite crystals from all these different assemblages have similar chemistry, with contents of CaO of 53.79–55.66 wt.%, $P_2O_5$ of 40.53–42.35 wt.%, and F of 2.18–3.46 wt.%. All apatites contain $La_2O_3+Ce_2O_3 > 0.5$ wt.%.

Fe-oxides occur as either euhedral grains or altered skeleton forms. Most large euhedral grains (>100 μm) contain carbonate, silicate glass, and apatite inclusions, and the rims of the Fe-oxides are embayed. Fe-oxides contain $TiO_2$ of 15.7-15.9 wt.%, FeO of 71.2-71.7 wt.% and are

high in $Al_2O_3$ of 2-5 wt.% and MgO of 0.1-0.7 wt.%. It is classified as aluminous ulvöspinel. Some Fe-oxides show alteration to hematite. The altered Fe-oxides have high $SiO_2$ of > 3 wt.% and low totals around 73-79 wt.% (Fig. 2c, Table 2).

The groundmass of the trachyandesite-trachyte is composed of microcrystal tabular feldspars of different Na-K ratios, varying from albite, anorthoclase, to sanidine ($Ab_{94.6\text{-}98.0}An_{0.7\text{-}4.6}Or_{0.3\text{-}2.2}$, $Ab_{52.5\text{-}72.1}An_{1.6\text{-}5.1}Or_{22.8\text{-}46.0}$, $Ab_{5.2}An_{0.7}Or_{94.1}$).

In the groundmass, there are carbonate nodules that contain microcrystalline ankerite, feldspar, and a minor amount of apatite, rutile, pyrite, and monazite within a carbonate rare circular feldspar shell. The carbonate enriched core of nodules contains about 60 vol.% carbonate grains (Fig. 4g). Pyrite grains are concentrated in the core and needle-shaped rutile and monazite crystals occur in the core of nodules, where feldspar crystals are larger (Fig. 4h). Ankerite grains are distributed interstitially among albite laths, crosscut albite laths, and also occur as inclusions within the albite (Fig. 4h). The carbonate-rich nodule is surrounded by a carbonate-poor shell consisted of microcrystalline feldspar (Fig. 4g).

### 3.2. Composition of the silicate glass

Silicate glass coexists with carbonate phases within the euhedral carbonate grains and inclusions hosted by biotite and ulvöspinel. The silicate glasses are divided into five types based on their appearance in the rock: 1) biotite-hosted silicate glass inclusions, 2) biotite-hosted coexisting silicate glass and carbonate inclusions, 3) ulvöspinel-hosted silicate glass inclusions, 4) silicate glass within euhedral pseudomorphic ankerite, and 5) individual silicate glass grains which contain abundant needle-shaped apatite and subhedral-anhedral Fe-oxide (Fig. 4b). Silicate glasses have 48 to 60 wt.% $SiO_2$ (Table 3, Figures 6a-g, Supplement II) and some are devitrified and form sericite.

For biotite-hosted silicate glass inclusions (Fig. 3h), the central part contains amorphous silicate glass with microcrystal apatite and submicron size Fe-oxides. The amorphous silicate glass has 57-60 wt.% $SiO_2$, 19-27 wt.% $Al_2O_3$, 1-2.5 wt.% FeO, 0.3-1.2 wt.% MgO, 0.2-0.6 wt.% CaO, 3.7-5 wt.% $Na_2O$, and 5-7.5 wt.% $K_2O$. The rim surrounding the amorphous silicate glass center is chemically homogenous with composition of lower $SiO_2$ (<52 wt.%) and higher $K_2O$ (~9 wt.%).

The silicate melt components in the rock exist in the following forms; silicate glass adjoining ankerite to form clusters (Fig. 2d), silicate glass rims surrounding multiple types of cores within the biotite-hosted inclusions (Figs. 3d, f, i, j), silicate glass in biotite-ankerite clusters (Fig. 4a), and individual silicate glass grains within the trachytic matrix (Fig. 4b). All these silicate components have similar chemistry with $SiO_2$ of 48-52 wt.%, $Al_2O_3$ of 26-33 wt.%, FeO of 2.6-3.4 wt.%, MgO of 1.1-1.8 wt.%), $K_2O$ of 8.8-10.6 wt.%), and less than 0.5 wt.% CaO and $Na_2O$. In the biotite-hosted silicate-ankerite inclusions, silicate glass surrounds ankerite to form a boundary between ankerite and biotite (Figs. 3d, f, i, j).

The silicate glass in ulvöspinel-hosted silicate inclusions show a relatively wide range of compositions with low $SiO_2$ of 41.5-53.3 wt.%, high FeO+MgO of 3.9-21.6 wt.%, total alkali of $K_2O + Na_2O$ = 0.3-4.8 wt.%, and oxide total is slightly low with 80.56-92.91 wt.% (Figs. 2b, 3a, and 6a-g).

The silicate glass in euhedral pseudomorphic ankerite (Fig. 2g) has low $SiO_2$ of 42.9-46.7 wt.%, high FeO+MgO of 20.2-26.8 wt.%, CaO around 1 w.t%, $K_2O$ between 1.4 to 4.8 wt.%, and $Na_2O$ less than 0.04 wt.%.

### 3.3. Composition of carbonate phases

Most carbonate components are classified as ankerite based on their compositions, but with slightly different Fe/Mg ratios. Based on their petrographic characters, the carbonate phases are divided into the following categories: (1) euhedral pseudomorphic ankerite grains, (2) spherical and dumbbell shape globule in trachyte matrix, (3) irregular shape inclusions in biotite and ulvöspinel, and (4) hexagonal shape inclusions in biotite. The representative chemical compositions of carbonate phases are listed in Table 4. Carbon and oxygen isotope ratios for the euhedral pseudomorphic phase are listed in Table 5.

**3.3.1** Euhedral pseudomorphic ankerite grains

Euhedral pseudomorphic ankerite grains represent the most unique feature in the trachyandesite-trachyte. They are distributed as individual grains or mineral clusters in the trachytic matrix (Fig. 2). Within the pseudomorphic grains, ankerite forms intergranular texture with crystalline Mg-rich crystals surrounded by the interstitial Fe-rich ankerite (Fig. 2f). The Mg-rich ankerites have MgO of 12.03-16.99 wt.%; CaO of 30.44-33.05 wt.%; FeO of 2.34-9.41 wt.%; and Fe-rich ankerites have MgO of 10.18-11.43 wt.%; CaO of 29.99-30.90 wt.%; FeO of

This is the peer-reviewed, final accepted version for American Mineralogist, published by the Mineralogical Society of America.
The published version is subject to change. Cite as Authors (Year) Title. American Mineralogist, in press.
DOI: https://doi.org/10.2138/am-2022-8007. http://www.minsocam.org/

297 10.87-13.32 wt.% (Table 4). Abundant euhedral apatite and subhedral to anhedral Fe-oxide are
298 included in the euhedral carbonate grains.

299 **3.3.2** Spherical globule in trachyte matrix

300 Spherical shaped carbonate globules reacted with trachytic magma and have embayed and
301 corroded rims. The ankerites in globules have significant zonation with a Mg-rich core and Fe-
302 rich rim (Fig. 2h). Micron size apatite needles and anhedral Fe-oxides are clustered within the
303 globules. Ankerite cores have high MgO (15.36-20.98 wt.%) and CaO (29.56-32.91 wt.%) and
304 low FeO (1.91-7.81 wt.%) and have multiple zoned centers. Fe-rich rims have low MgO (12.33-
305 15.01 wt.%) and CaO (27.68-31.27 wt.%) and high FeO (9.45-10.71 wt.%) contents.

306 **3.3.3** Irregular shaped carbonate inclusions hosted in biotite and ulvöspinel

307 Most carbonate inclusions in biotite are zoned and characterized by relatively high MgO
308 (10.17-14.44 wt.%), FeO (10.76-15.26 wt.%), $Al_2O_3$ (0.01-2.09 wt.%), MnO (0.44-2.80 wt.%),
309 and variable CaO (23.89-33.33 wt.%) (Table 4). Some carbonate inclusions contain euhedral
310 albite and anorthoclase, subhedral Fe-oxide, silicate glass relicts, and ankerite (Fig. 3f). Some
311 carbonate inclusions contain ankerite with apatite and Fe-oxide microcrystals surrounded by
312 silicate glass rim (Fig. 3j).

313 The carbonate inclusions hosted by ulvöspinel contain relatively low MgO (9.35 – 11.94
314 wt.%), $Al_2O_3$ (0 – 0.06 wt.%), MnO (0.38 – 0.74 wt.%), high FeO (14.27 – 18.22 wt.%), and
315 variable CaO (Table 4). Their FeO contents are higher than carbonate inclusions hosted by
316 biotite (Figs. 6h, i).

317 **3.3.4 Hexagonal carbonate inclusions hosted in biotite**

318 Hexagonal shape inclusions in biotite have silicate glass surrounding different types of
319 cores. Some ankerite cores contain abundant apatite, Fe-oxide, and occasional monazite (Figs.
320 3d). Mg-rich (MgO 12.6-13 wt.%, FeO 8.6-12 wt.%, CaO 31.6-32.4 wt.%) and Fe-rich (MgO
321 7.8-11.5 wt.%, FeO 12.3-17.9 wt.%, CaO 28.2-30.7 wt.%) ankerite show irregular patches in the
322 inclusions (Fig. 3i). Some hexagonal inclusions contain zoned carbonate with very thin silicate
323 glass rim (Fig. 3e). The core is Mg-rich ankerite (MgO 13.9-14.4 wt.%, FeO 9.7-11.3 wt.%, CaO
324 28.4-29.1 wt.%) with vesicles. Rims of carbonate are more Fe-rich (MgO 12.1-12.7 wt.%, FeO
325 12.8-13.3 wt.%, CaO 29.4-30.5 wt.%). Some cores contain euhedral apatite crystals (Fig. 3g).

326 **3.3.5 Carbon and oxygen isotopes**

This is the peer-reviewed, final accepted version for American Mineralogist, published by the Mineralogical Society of America.
The published version is subject to change. Cite as Authors (Year) Title. American Mineralogist, in press.
DOI: https://doi.org/10.2138/am-2022-8007. http://www.minsocam.org/

As shown in Fig. 7 and Table 5, fourteen euhedral pseudomorphic ankerite grains from 4 samples have $\delta^{13}C$ (VPDB, ‰) ranging from -3.98 to -5.76, and $\delta^{18}O$ (SMOW, ‰) from 4.43 to 11.49. Most C and O isotope data (11 out of 14, $\delta^{13}C \sim$ -4.65 to -5.76; $\delta^{18}O \sim$ 6.5 to 9.5) plot within the field of primary igneous carbonatites (PIC) as defined by Keller & Hoefs (1995). Two samples have slightly lower $\delta^{18}O$ ($\delta^{13}C \sim$ -5.18 to -5.26; $\delta^{18}O \sim$ 4.4 to 5.25) and one sample has $\delta^{13}C$ of -3.98 and $\delta^{18}O$ of 11.49. Overall, the carbonates have much lower $\delta^{18}O$ values than those associated with Phanerozoic limestones.

## 4. Discussion

### 4.1 Tectonic setting and volatile contents

The Sea of Japan is a back-arc basin with a thick basaltic oceanic crust (14 km) (Hirahara et al., 2015), and is influenced by different mechanisms of mantle convection (subduction along a convergent margin, buoyant mantle upwelling, and plate spreading) (e.g. Druken et al. 2011, 2014; Price et al. 2017). Back-arc volcanic rocks are enriched in LILE, Th, U, and such distinctive trace element signatures of back-arc magma are usually linked to the volatile flux derived from dehydration reactions in the subducting slab (Pearce et al., 1995; Elliott et al., 1997; Spandler and Pirard, 2013; Bebout and Penniston-Dorland, 2016). The magma developed in this environment contains greater concentrations of volatiles and has higher $CO_2/H_20$ ratios than MORB, which suggests the involvement of a slab-derived volatile component (Weaver, 1991; Troll et al., 2012; Kimura et al., 2014). As the volatile flux moves into the warm interior of the mantle wedge, increasing temperature can form supercritical melts/fluids by hydrous melting and (Hall and Kincaid, 2001; Grove et al., 2002). The greater degree of melting of hydrous metasomatized mantle at an unusually high temperature played a major role during the formation of the Sea of Japan back-arc (Hirahara et al., 2015). Volatile flux liberated from the upper part of the subducting slab contains high contents of $H_2O$, Cl, S, $CO_2$ and can carry a significant amount of water-soluble trace elements, such as K, Rb, Cs, U, Pb, Sr, Ba, into the overlying mantle wedge (Jarrard, 2003; Staudigel, 2003; Spandler and Pirard, 2013).

The extensional environment enhances the release of volatiles and any subsequent melt ascending into the lower pressure zone in this back-arc volcanic system (Laporte et al. 2014; Zhang et al., 2017). The initiation of melting relative to the volatile-saturated solidus can happen in this environment (Mibe et al., 2004; Kelley et al., 2006), and the ascending material can

induce partial melting in the mantle wedge. Based on its location in the back-arc, the Ulleung Island volcanic system is expected to erupt volatile-rich magma, and the rocks do contain high contents of LILE, Th, U, Nb, and LREE (Brenna et al., 2014). The reactive porous flow of the volatile-rich supercritical materials, carbon flux, moving through the mantle wedge and the lower crust may be the most likely mechanism to generate the Ulleung Island mafic volcanic system. This mantle wedge may be composed of carbonated eclogite. The carbon flux induced partial melting and generated alkali mafic magma with high incompatible trace elements. An isotope study of Ulleung volcanic rocks suggested that magmatism was correlated with wet upwelling of slab fluids in the mantle transition zone (Choi, 2020).

Carbonate metasomatism in the mantle can lower the solidus and generate partial melts that are highly alkalic in nature (Sweeney, 1994; Lee and Wyllie, 1998; Dasgupta and Hirschmann, 2007, Ghosh et al., 2009; Chen et al. 2013, Loges et al., 2019). The carbonatite correlated oceanic-island magmatic systems, such as the Canary Islands, Cape Verde, Gough Island, Honshu, Rose Island, Trindade, and Tristan de Cunha, were all developed from hydrous melts (Troll and Schmincke, 2002; Taylor and Martinez, 2003; Pilet et al., 2008; Hildner et al., 2011; Sliwinski et al., 2015; Jerrery and Gertisser, 2018).

### 4.2 Euhedral pseudomorphic ankerite grains

The occurrence of euhedral ankerite is the most puzzling aspect of this study (Fig. 2). It is not possible to crystallize these euhedral carbonate minerals from a trachytic melt. At least no example of this process has yet to be reported. These euhedral ankerite grains did not form by post-magmatic carbonate fluid alteration, because (1) fresh unaltered and euhedral biotite are embedded in and crosscut the ankerite grains (Fig. 2a); (2) euhedral pseudomorphic ankerite is included in biotite (Fig. 3b); (3) no carbonate alteration and no carbonate veins are observed in the groundmass; (4) multi-stage crystallization occurred within these euhedral ankerite grains (Fig. 2f); (5) euhedral apatite and rutile coexist with ankerite; (6) plagioclase phenocrysts are altered and contain ankerite. If these euhedral ankerite grains were subjected to carbonate fluid alteration in the near-surface environment, biotite phenocrysts and the groundmass feldspars should inevitably be altered as well.

Some euhedral ankerite grains show prismatic and tabular forms (Fig. 2), and some of the euhedral ankerite grains exhibit the basal cross-section of pyroxene (Fig. 2g). The detailed

mineralogical and petrological observations show that these euhedral ankerite grains were resorbed along the rim and fractures by the trachytic melt (Figs. 2d-f). The euhedral ankerite grains are not single carbonate crystals but are composed of multiple euhedral Mg-rich ankerites with interstitial Fe-rich ankerite (Fig. 2f). Euhedral apatite and subhedral ulvöspinel are included in the euhedral ankerite grains (Fig. 3a).

The carbon and oxygen isotope compositions of these euhedral carbonate grains overlap with those of typical carbonatites in a range of $\delta^{13}C_{VPDB}$ -3.98 to -5.76 and $\delta^{18}O_{SMOW}$ 4.43 to 11.49 (Fig. 7). A majority of the samples are in the range of $\delta^{13}C$ -4.65 to -5.76 and $\delta^{18}O$ 6.77 to 9.48. Two of samples have slightly lower $\delta^{18}O$ ($\delta^{18}O \sim 4.4$ to 5.2) and one sample has $\delta^{18}O$ of 11.49 (Fig. 7b). $\delta^{18}O$ of carbonatites from different areas vary in the range from 5 to 30 (Bell and Simonetti, 2010), which may reflect their source characteristics and/or alteration. The carbon and oxygen isotopes of our samples are clearly different from those of sedimentary carbonates (Fig. 7). Phanerozoic limestones mainly have positive $\delta^{13}C$ (Bell and Simonetti, 2010), whereas biogenic carbonates have $\delta^{13}C$ ranging from -5 to -35 (Maeyama et al., 2020). The carbon and oxygen isotopes from hydrothermal calcite show an extensive range for both $\delta^{13}C$ (5 to -30) and $\delta^{18}O$ (0 to 25) (Whitley et al., 2019). Even though some skarns from Japan fall in the field of "igneous calcite", the majority of hydrothermal calcites have high $\delta^{18}O_{SMOW}$ (> 10) (Whitley et al., 2019). Since the development of pseudomorphic carbonate involved a substitution process, then variable C-O isotope ratios are expected. The low $\delta^{18}O$ values of the studied samples may be attributed to the mixing of water in the flux. The higher $\delta^{18}O$ values may be the result of 1) high temperature carbonate fractionation of a carbonatite-like melt (Maeyamaa et al., 2020; Ray and Ramesh, 2000), 2) interaction between the carbon flux and ambient materials from mantle to the magma chamber, and 3) a later-stage influence or alteration from hydrothermal fluid; a similar feature was observed in natrocarbonatites from Oldoinyo Lengai (Keller and Hoefs, 1995). The C-O isotope compositions from the colloform carbonates in Section 5 are consistent with those of hydrothermal origin ($\delta^{13}C_{VPDB} \sim$ -0.8 to -1.4 and $\delta^{18}O_{SMOW} \sim$ 17.6 to 18.6, Supplement I); this hydrothermal event may have also affected the rocks in the other sections. Thus, the carbon and oxygen isotope ratios reported here provide convincing evidence that supports an igneous origin of these carbonate grains.

The Fe/Mg ratio in the pseudomorphic ankerite ranges from 0.5 to 1.3. Experimental works conducted at high pressure with carbonated peridotite indicate that the resulting

carbonates are mostly Mg-rich in nature (Wallace and Green, 1988; Falloon and Green, 1989; Dasgupta and Hirschmann, 2006; Litasov and Ohtani, 2009). The melt composition corresponds to that of magnesiocarbonatite with Ca-Mg ratio negatively correlated with pressure and temperature (Ghosh et al., 2009). Alternatively, Fe-rich carbonatites are also typically associated with late-stage carbonatite melt evolution (Simonetti and Bell, 1994; Simonetti et al., 1995; Prokopyev et al., 2016). In this case, the Fe may derive from the original mafic mineral (either pyroxene or amphibole) that is being replaced by the carbonate phases in the volatile-rich environment. During this replacement, the Fe was compatible with carbonate and formed ankerite. This process will not change the C and O isotope compositions of the carbonate pseudomorphs since both the original minerals and carbonate are of mantle origin. Consequently, these grains are classified as carbonate pseudomorphic grains. The preexisting pyroxene and/or amphibole were replaced by carbonate melt in the lower crust or the bottom of a fractionated magma chamber and then incorporated in the trachytic magma. The contact zone between ankerite and biotite is K-silicate glass, with a composition similar to muscovite (Figs. 3, 4a). The K-silicate glass can form from the high-K silicate melt. Alternatively, it may be related to the alteration of biotite by the fluid within carbonate melt. In either case, the carbonate phases were formed from high volatile and high-temperature carbonate melt.

### 4.3 Hexagonal shape inclusions in biotite

The hexagonal-shaped carbonate and carbonate-silicate inclusions in biotite (Fig. 3) provide additional evidence for the high volatile content of the carbonate melt. There are voids in the cores of the biotite-hosted ankerite inclusions (Figs 3e, i), which might form from escaped gas. The hexagonal shape inclusions in biotite could be negative crystal shape inclusions, the included melt/fluid acquired a shape imposed by the crystal habits of the host mineral. Negative crystal shape inclusions represent the primary inclusions of the host crystals (Benz and Neumann, 2014). The zoning character of the hexagonal ankerite inclusion is similar to those of the carbonate globules (Fig. 2h). These inclusions may represent the low viscosity carbonate melt or supercritical fluid that was enclosed by biotite. Due to the high fluid content and the corresponding low viscosity of carbonate melt, the captured melt in biotite was forced to follow the crystal structure and formed the hexagonal shape following the biotite symmetry. The carbonate-silicate negative crystal shape inclusions hosted by garnet were reported in granitoids

and experimental studies (Safonov et al., 2020; Hermann et al., 2013). This is the first reported hexagonal shape carbonate melt inclusions in biotite.

The high Ti content of the biotite is consistent with the alkali-rich character of the trachytic volcanic system (Chukanov et al., 2008). The biotite was an early crystallized mineral in the trachytic magma chamber. The carbonate melt inclusions in biotite indicate that the recharging of carbon flux into the magma chamber could cause the eruptions of the Ulleung Island volcanic system.

### 4.4 Carbonate in plagioclase and carbonate nodules in the groundmass

Most of the labradorite-bytownite phenocrysts are altered. The assemblage of anhedral ankerite, albite, quartz, and the relicts of plagioclase replaced the original feldspar crystals (Figs. 4e, f). Some plagioclases have altered sericite core surrounded by ankerite and albite intergrowths. A thin layer of albite usually jackets the altered feldspar. This mineral assemblage with plagioclase indicates that the carbonate-silicate alteration took place before the feldspars were captured in trachyte magma. Some cores of anorthoclase crystals also contain ankerite, which indicates the existence of carbonate melt in the trachyte magma during the early stage of anorthoclase crystallization.

Carbonate concentrated in nodules is another indication of the carbon-rich nature of this trachyte magma (Fig. 4g). Pyrite and monazite are gathered in the core area because of the concentration of S and REE in the later stage of crystallization.

### 4.5 Geochemical characters of the carbonate components

Abundant apatite, ulvöspinel, and a few rutile crystals occur in ankerite. Apatite contains more than 0.5 wt.% LREE, whereas the ankerite contains less than 0.1 wt.% LREE (Table 2). Experimental studies of phosphorus-containing $CaCO_3$ melt demonstrate that the solubility of phosphorus decreases with increasing partial pressure of $CO_2$ and decreasing temperature (Baker and Wyllie 1992). Apatite crystalizes before the carbonate phases in carbonate melt and REEs are much more compatible in phosphate minerals than in carbonate minerals (Ryabchikov et al., 1993; Veksler et al., 2012).

The Fe-Mg contents in ankerite are different when comparing the carbonate inclusions hosted by ulvöspinel to those hosted by biotite. Ulvöspinel-hosted ankerite has more FeO and

biotite-hosted ankerite has more MgO and $Al_2O_3$ (Figs. 6h, i). These changes can correlate with the diffusive reaction between the included melt and its host, which also support the suggestion that the Fe represents a residual component from the replaced phase in the pseudomorphic carbonate grains. Non-equilibrium growth of the mineral on the inclusion walls (typically with slightly different compositions) can modify the chemical composition of both the trapped fluid and the host mineral (Frezzotti and Ferrando, 2015). Nevertheless, the carbonate inclusions are important indicators of the evolution of carbonate melt in Ulleung Island.

### 4.6 Features of silicate melt in Ulleung Island trachytic rocks

Ulleung Island trachytes contain abundant carbonate-silicate grains (Fig. 2d) and carbonate-silicate inclusions (Fig. 3). The silicate glass in ulvöspinel-hosted inclusions and euhedral pseudomorphic carbonate grains show chemical differences when compared to the biotite-hosted silicate inclusions (Figs. 6a-g). Ulvöspinel-hosted silicate inclusions are enriched in MgO and FeO with significantly higher $TiO_2$ (0.17–0.70 wt.%) (Fig. 6e; Table 2) and CaO (0.31–2.8wt.%) contents; while biotite-hosted silicate inclusions are enriched in $K_2O$-$Na_2O$ and $Al_2O_3$, but have very low MgO and FeO contents (Fig. 6a-g). These features suggest that these two types of silicate melt inclusions record melt composition at different stages of magma evolution. The silicate inclusions in ulvöspinel and euhedral pseudomorphic carbonate grains captured the deep primary mafic melt and the chemical evolution trend from these inclusions record magmatic evolution.

The different chemical characteristics of silicate melt in biotite and ulvöspinel hosted inclusions and in euhedral pseudomorphic carbonate grains may correspond to their origin. Chemical variation within the low $SiO_2$ group may represent the changes in melt chemistry within the magma chamber. Based on the mineral properties for hosts of the low $SiO_2$ group silicate melt, such as the xenocrystal feature of the euhedral pseudomorphic carbonate grains, the alteration in plagioclase, and the corrosion feature of the Fe-oxides, the hosts of low $SiO_2$ silicate melt were formed previous to the intrusion of trachytic magma, and the low $SiO_2$ silicate melt may represent the recharging mafic melt in the magma chamber. The biotite-hosted silicate melt inclusions record the evolved trachytic magma.

The carbonate-silicate inclusions in biotite (Fig. 3), especially the hexagonal shape inclusions (Fig. 3), and the nodule with intergrown ankerite and feldspar (Fig. 4g) may record the

features of the immiscible carbonate-silicate melt. The exsolution of carbonate and silicate melts is documented in both experimental studies (Kiseeva et al., 2012; Bulatov et al., 2014; Shatskiy et al., 2021) and natural samples (Kogarko et al., 2001; Kelley et al., 2005; Guzmics et al., 2011; De Ignacio et al., 2012). The experimental carbonate melt contains a high amount of $Na_2O$+$K_2O$ (Chen et al., 2013; Kiseeva et al., 2013; Bolatove et al., 2014; Litasov et al., 2020; Shatskiy et al., 2021). There is a clear difference in the studied carbonate-silicate inclusions reported here compared to those experimental results. The carbonate components hosted in biotite have low $K_2O$+$Na_2O$, whereas the silicate compositions hosted in biotite are enriched in $K_2O$+$Na_2O$ with very low CaO, MgO, and FeO (Table 3, 4). The relatively complete chemical separation of the carbonate and silicate might correspond to the high volatile flux in the melt (Macdonald et al., 1993). Some carbonate inclusions in biotite and the carbonate globules in the rocks show the Liesegang phenomena of periodic precipitation (Figs. 2h, 4e). The formation of these zoning features occurs in a relatively low viscosity melt or supercritical fluid, by the processes such as diffusional mass transport and/or the periodic growth of minerals according to the composition of the trapped materials. These zoning patterns might also record the variation of physical conditions (P-T etc.) of the low viscosity melt (Frezzotti and Ferrando, 2015). The lower viscosity of the peralkaline felsic magma has been confirmed in the Atlantic Ocean volcanic systems, the peralkaline felsic magmas exhibit lower viscosities than the metaluminous equivalents (Jeffery et al., 2018).

Melting point of carbonate decreases in the order of calcite ($CaCO_3$) > MgO-rich calcite > magnesite ($MgCO_3$) > siderite ($FeCO_3$) (Irving and Wyllie, 1975), so the Mg and Fe contents of crystallized carbonates increase with increasing degree of crystallization (Le Bas, 2008; Zhang et al., 2017). The observed formation sequences of carbonate in this study exhibit the same crystallization trend, e.g., euhedral Mg-rich ankerite dispersing within the interstitial anhedral Fe-rich ankerite in the euhedral pseudomorphic carbonate grains (Fig. 2f), zoned Mg-rich ankerite jacketed by Fe-rich ankerite in the spherical carbonate globule (Fig. 2h), and zoned carbonate phase included in negative crystal shape inclusions (Fig. 3e). The carbonate minerals in this study were crystalized from a carbonatite-like melt.

### 4.7 Carbon flux

543 Carbonate phases in Ulleung island trachyte are evidence of the circulation of high
544 volatile components, as the carbon flux, in the back-arc basin. The compositions of ulvöspinel-
545 hosted silicate melt inclusions likely represent a MgO, FeO, $Al_2O_3$, CaO, and $TiO_2$-rich and
546 $Na_2O+K_2O$-poor initial silicate melt, and those of ulvöspinel-hosted carbonate melt inclusions
547 may represent a FeO-rich and MgO, $Al_2O_3$, MnO-deficient initial carbonate melt. Experimental
548 work has demonstrated that felsic glass, with a composition of trachyte, could be in equilibrium
549 with upper mantle rocks at temperatures as low as 850°C and pressures between 10 and 20 kbar
550 in the presence of $CO_2$ and $H_2O$ fluid (Draper & Green, 1997). The ultimate origin of the $CO_2$
551 and $H_2O$ might be from recycled material derived from a subducting slab at a convergent plate
552 margin (Wood et al., 1990; Coltori et al., 1999). The direct information about natural C-H-O
553 fluids usually obtained from the study of fluid-inclusions in mantle-derived diamond (Schrauder
554 and Navon, 1994). These aqueous fluids produced by slab devolatilization can dissolve a
555 considerable amount of carbon (Frezzotti et al., 2011; Li, 2017), thus the volatile-rich fluids have
556 been referred to as "carbon flux" in this study.
557 Carbon flux should play a critical role during the partial melting of the mantle wedge above
558 the subducting slab (Dasgupta et al., 2007). Based on the experimental studies, carbonate melt
559 can form from: (1) low degree partial melts directly from the mantle source (Wallace and Green,
560 1988; Green and Wallace, 1988; Yaxley et al., 1991; Dalton and Presnall, 1998); (2) fractional
561 crystallization of anatectic melts generated in the wet mantle wedge (Lee et al., 1994; Lee and
562 Wyllie, 1994, 1998; Pearce et al., 1995); (3) liquid immiscibility of $CO_2$-rich alkaline silicate
563 magma (Kjarsgaard and Hamilton, 1989; Nielsen et al. 1997; Kjarsgaard, 1998; Sokolov et al.
564 1999; Rass and Plechov 2000; Mitchell, 2009; Guzmics et al. 2011); (4) Carbonate-
565 metasomatism is documented in many studies of eclogitic xenoliths and massive eclogite terrains
566 (e.g., Pyle and Haggerty 1994, Kiseeva et al., 2012; Johns et al., 2013), and it implies an active
567 role of metasomatic carbonate fluids in subduction zones (Selverstone et al. 1992). The
568 carbonated melt from South China Sea indicates that the melt was generated from a carbonated
569 eclogite source (Zhang et al., 2017). The models of low degree partial melting and fractional
570 crystallization of anatectic melt of the carbonated peridotite usually generate high Mg carbonate
571 melt, which is different from the composition of observed ankerite. However, the pseudomorphic
572 carbonate grains formed from the substitution process. The Fe from the original minerals may
573 have incorporated into carbonate melt to generate the high Fe carbonate phases.

This is the peer-reviewed, final accepted version for American Mineralogist, published by the Mineralogical Society of America.
The published version is subject to change. Cite as Authors (Year) Title. American Mineralogist, in press.
DOI: https://doi.org/10.2138/am-2022-8007. http://www.minsocam.org/

574 The $CO_2$ and $H_2O$ originated from the recycled components of a subducting slab and these
575 fluids (the carbon flux) can infiltrate and be reheated by the overlying mantle wedge (Yaxley and
576 Brey 2004; Dasgupta and Hirschmann, 2010; Creon et al., 2017). Since the low viscosity of
577 carbonate melt is favorable to crystallization and accumulation, the higher activity of carbonate
578 melt is beneficial to the separation of volatile phases, thus the bulk-rock geochemical
579 compositions of carbonate melts may not represent the components of its parent magma
580 (Woolley and Church, 2005). As discussed previously, the replacement of the original mineral
581 phases (pyroxene or amphibole) by the carbonatitic melt could also change the chemistry of the
582 melt. This process explains the compositional variability of carbonate melts and the coexistence
583 of silicate and carbonate melts. Hence, the origin and evolution of the carbonate melt can
584 generate different mineral phases, micro-textures, and micro-chemical compositions.
585
586 **4.8 Melt development model**
587 With the injection of subduction released carbonate melts/liquids in the mantle wedge
588 and lower crust in the back-arc extensional environment, a magma chamber could form in the
589 lower crust (Fig. 8). The early portion of silica under-saturated melt could rise into the upper
590 crust and erupt the early episodes of mafic units (Fig. 1c). The recharge of carbon flux in the
591 magma chamber may provide the energy and materials for multiple eruptions. The coexisting
592 carbonate-silicate melt inclusions, both irregular and hexagonal shapes, in biotite (Fig. 3) likely
593 record the separation of immiscible carbonate-silicate melt during the magma ascent (Dasgupta
594 et al. 2007; Harmer, 1999; Jones et al. 2013).
595 If these carbonate-silicate melts stall, they can segregate carbonate melt/fluid and cause
596 percolation of carbonate material in the rocks (Wyllie et al., 1996). The carbonate dissolution in
597 the dehydrating fluids can be preserved as ionic carbon species (Frezzotti et al., 2011; Sverjensky
598 et al., 2014), and the fluids may cause percolation of carbonate material in early crystallized
599 minerals (Hammouda and Laporte 2000) (Supplement I). The fractionation process in the magma
600 chamber might generate a mushy zone containing accumulate crystals with residual melts
601 (Hildreth, 1981; Wolff, 1985; Bachmann and Bergantz, 2004). In this case, the accumulate
602 crystals were pyroxene and plagioclase. Larger volumes of crystalline phases may accumulate in
603 the lower magma chamber due to the low viscosity of the volatile-rich nature of the magma. The
604 separated pyroxene and plagioclase crystals could form a mushy section in the lower magma

chamber, whereas the upper magma chamber evolved to a more felsic zone. The new batches of carbon flux recharged the magma chamber and produced a mushy zone impregnated by carbonate melts. The percolation of carbonate components replaced the original mineral phases and formed pseudomorphic ankerite grains (Fig. 8). When the magma chamber received large recharge and built up enough energy, the recharged melt can penetrate the upper more felsic trachyte zone of magma chamber and erupt. The recharged melt captured the euhedral pseudomorphic ankerite grains and partially altered feldspars in the trachytic magma zone. This model can better explain that the euhedral pseudomorphic carbonate grains are main in trachyandesite and trachybasalt but are rare in trachyte. The fluid-melt feature (supercritical fluid) of the carbon flux has been preserved in the Ulleung island trachytic rocks in a variety of ways, e.g., the multi crystallization phases in euhedral pseudomorphic carbonate grains (Fig. 2f), the zoned ankerites in spherical carbonate globule (Fig. 2h), the zoning pattern of ankerite in negative crystal shape inclusions and irregular inclusions in biotite (Fig. 3), and the immiscible ankerite-feldspar nodule (Fig. 4g). Carbon flux infiltrating and impregnating the gabbroic lower crust might also be suitable to the environment of forming euhedral pseudomorphic carbonate grains. However, the mushy magma chamber model may more easily explain the repeated eruptions at Ulleung island.

The volcanic rocks from South China Sea Site U1431 exhibit a continuous transition from carbonated silicate melt to alkali silicate melt and represent carbonated silicate fluids passing through the lithosphere via reactive infiltration. These carbonated silicate melts were interpreted as being derived from deep carbonated eclogite (Zhang et al., 2017). The Ulleung Island volcanic rocks exhibit similar geochemical features to those volcanic systems in the South China Sea (Brenna et al., 2014; Zhang et al., 2017), indicating that the activity of carbon fluxes should be a common process in back-arc basins (Wood et al., 1990; Coltori et al., 1999; Johnston et al., 2011; Kelemen and Manning, 2015). The volcanic system in Ulleung Island preserves extraordinary evidence of the carbon flux activity within the lower crust. The recycled carbon from the subducted slab can be stored within the lower crust through the replacement of silicate minerals. The calculation of carbon circulation in the earth system may need to consider this parameter in future mass balance model calculations.

## 5. Conclusions

Ulleung Island volcanic rocks are an alkaline series consisting of trachybasalt, trachyandesite, trachyte, and phonolite. Abundant euhedral pseudomorphic carbonate grains, spherical carbonate globules, and carbonate-silicate melt inclusions occur in the rocks. Based on the data reported here, we infer that subduction related carbon flux metasomatism provides a notable contribution to the formation of the high alkali volcanism. The trachyandesite, which contains the most of euhedral pseudomorphic carbonate grains, spherical and dumbbell shape carbonate globules with zoning texture, ulvöspinel-hosted and biotite-hosted carbonate melt inclusions, and hexagonal shape coexisting carbonate-silicate melt inclusions, in the Ulleung Island volcanic rocks, represents the recharging melt feeding the magma chamber.

The euhedral pseudomorphic carbonate grains and carbonate melt inclusions are of magmatic origin. The carbon flux, which was released from the subducted plate, was transported in the mantle and lower crust and generated mafic melt. The carbon flux also caused the carbonate metasomatism in the crust or preexisting magma chamber, generated the pseudomorphic carbonate grains, altered plagioclase, and formed carbonate-silicate melt inclusions in biotite and ulvöspinel. The compositions of ulvöspinel-hosted silicate melt inclusions likely represent a MgO, FeO, $Al_2O_3$, CaO, $TiO_2$-rich, and $Na_2O$+$K_2O$-poor primary silicate melt at Ulleung Island. The geochemical characters of coexisting silicate-carbonate melt inclusions indicate that they recorded the processes of silicate-carbonate melt immiscibility.

The euhedral pseudomorphic carbonate grains and hexagonal shape melt inclusions in biotite are described for the first time in this back-arc volcanic region. The carbon flux generated from the subducted oceanic crust formed these non-traditional features and played a fundamental role in the origin of alkali silicate melts in the back-arc volcanism.

## 6. Implications

The volcanic system in Ulleung Island preserves extraordinary evidence of carbon flux activity within the lower crust. The carbonate phases in Ulleung Island samples formed from carbonate melt generated by the carbon flux from the subducted oceanic slab. The lower crust may store this recycled carbon by replacing silicate minerals. These observations suggest that there may be a significant accumulation of carbon in carbonates in some back-arc settings that should be accounted for in any future modeling of terrestrial carbon circulation and recycling. If the recycled carbon is stored in the crust, magmas rising from the mantle may include some of

667 the carbonate liberating $CO_2$; thus, highly explosive eruptions can increase volcanic risk in
668 highly populated areas. Additionally, this study helps improve our understanding of back-arc
669 basin volcanism, and combined with geophysical studies, it can provide a better petrologic and
670 tectonic framework for the back-arc setting.
671
672 **Acknowledgments**
673 This work was supported by the programs of Guangdong Introducing Innovative and
674 Entrepreneurial Teams, Zhujiang Talent Project Foundation of Guangdong Province (Grant no:
675 2017ZT07Z066), Major Projects of the National Natural Science Foundation of China
676 (41590863), Fundamental Research Funds for Young teacher development project (32110-
677 31610351), and Double first-class guidance project (32110-18841213). Seung-Gu Lee and Tae
678 Jong Lee were supported by Principal Research Fund GP2021-006 and GP2021-010,
679 respectively, provided by Korea Institute of Geoscience and Mineral Resources. Shichun Huang
680 was supported by NSF grant (EAR-1942042). Carbon and oxygen isotope analyses were
681 supported by Ganqing Jiang (UNLV-LVIS). We also appreciate thoughtful and constructive
682 comments from reviewers and editors of American Mineralogist.

## References

Alt, J.C., and Teagle, D.A.H. (1999) The uptake of carbon during alteration of ocean crust. Geochimica et Cosmochimica Acta, 63(10), 1527–1535.

Arai, F., Oba, T., Kitazato, H., Horibe, Y., and Machida, H. (1981) Late Quaternary tephrochronology and paleo-oceanography of the sediments of the Japan Sea, The Quaternary Research, 20, 209–230.

Bach, W., Alt, J.C., Niu, Y., Humphris, S.E., Erzinger, J., and Dick, H.J. (2001) The geochemical consequences of late-stage low-grade alteration of lower ocean crust at the SW Indian Ridge: Results from ODP Hole 735B (Leg 176). Geochimica et Cosmochimica Acta, 65(19), 3267–3287.

Bachmann, O., and Bergantz, G.W. (2008) Rhyolites and their source mushes across tectonic settings. Journal of Petrology, 49,2277-2285.

Baker, M.B., and Wyllie, P.J. (1992) High-pressure apatite solubility in carbonate-rich liquids: implications for mantle metasomatism. Geochimica et Cosmochimica Acta, 56(9), 3409–3422.

Bebout, G.E. (1996) Volatile transfer and recycling at convergent margins: Mass-balance and insights from high-P/T metamorphic rocks, in Subduction Top to Bottom, Geophys. Mon., vol. 96, edited by G. E. Bebout et al., pp. 179–193, AGU, Washington, D.C.

Bebout, G.E. (2007) Metamorphic chemical geodynamics of subduction zones. Earth and Planetary Science Letters, 260, 373–393.

Bebout, G.E., and Penniston-Dorland, S.C. (2016) Fluid and mass transfer at subduction interfaces–the field metamorphic record. Lithos, 240–243, 228–258.

Bell, K. and Simonetti, A. (2010) Source of parental melts to carbonatites–critical isotopic constraints. Mineralogy and Petrology, 98, 77–89

Benz, K.W., and Neumann, W. (2014) Introduction to Crystal Growth and Characterization, Wiley, p438. DOI:10.1002/9783527689248.

Brandl, P.A., Genske, F.S., Beier, C., Haase, K. M., Sprung, P., and Krumm, S. (2015) Magmatic Evidence for Carbonate Metasomatism in the Lithospheric Mantle underneath the Ohře (Eger) Rift. Journal of Petrology, 56(9), 1743–1774.

Brenna, M., Price, R.C., Cronin, S.J., Smith, I.E., Sohn, Y.K., Kim, G.B., and Maas, R. (2014) Final Magma Storage Depth Modulation of Explosivity and Trachyte–Phonolite Genesis at

an Intraplate Volcano: a Case Study from Ulleung Island, South Korea. Journal of Petrology, 55(4), 709–747.

Bulatov, V.K., Brey, G.P., Girnis, A.V., Gerdes, A., Höfer, H.E. (2014) Carbonated sediment–peridotite interaction and melting at 7.5–12 GPa, Lithos 200–201 (2014) 368–385

Burton, M.R., Sawyer, G.M., and Granieri, D. (2013) Deep carbon emissions from volcanoes. Reviews in Mineralogy and Geochemistry, 75, 323–354.

Chen, S., Lee, S., Lee, T.J., Lee, Y., and Liu, J. (2018) Multi-stage magmatic plumbing system of the volcano: A case study from Ulleung Island, South Korea. Lithos, 201–215.

Chen W., Kamenetsky, V.S., and Antonio Simonetti, A., (2013) Evidence for the alkaline nature of parental carbonatite melts at Oka complex in Canada, NATURE COMMUNICATIONS 4:2687, DOI: 10.1038/ncomms3687

Choi, S.H. (2020) Geochemistry and petrogenesis of Quaternary volcanic rocks from Ulleung Island, South Korea. Lithos, https://doi.org/10.1016/j.lithos.2020.105874

Chukanov, N.V., Rozenberg, K.A., Rastsvetaeva, R.K., and Möckel, S. (2008) New data on titanium-rich biotite, a problem of "wodanite". New Data on Minerals, 43, 72-77

Coltorti, M., Bonadiman, C., Hinton, R.W., Siena, F., and Upton, B.G. (1999) Carbonatite Metasomatism of the Oceanic Upper Mantle: Evidence from Clinopyroxenes and Glasses in Ultramafic Xenoliths of Grande Comore, Indian Ocean. Journal of Petrology, 40(1), 133–165.

Creon, L., Rouchon, V., Youssef, S., Rosenberg, E., Delpech, G., Szabo, C., and Guyot, F. (2017) Highly $CO_2$ -supersaturated melts in the Pannonian lithospheric mantle – A transient carbon reservoir? Lithos, 519–533.

Dalton, J.A., and Presnall, D.C. (1998) Carbonatitic melts along the solidus of model lherzolite in the system CaO-MgO-$Al_2O_3$-$SiO_2$-$CO_2$ from 3 to 7 GPa. Contributions to Mineralogy and Petrology, 131(2–3), 123–135.

Dasgupta, R. (2013) Ingassing, storage, and outgassing of terrestrial carbon through geologic time. Reviews in Mineralogy and Geochemistry, 75, 183–229.

Dasgupta, R. and Hirschmann, M.M. (2006) Melting in the Earth's deep upper mantle caused by carbon dioxide. Nature 440, 659–662.

Dasgupta, R. and Hirschmann, M.M. (2007) Effect of variable carbonate concentration on the solidus of mantle peridotite. Am. Mineral. 92, 370–379.

Dasgupta, R., and Hirschmann, M.M. (2010) The deep carbon cycle and melting in Earth's interior. Earth and Planetary Science Letters, 298(1), 1–13.

Dasgupta, R., Hirschmann, M.M., Mcdonough, W.F., Spiegelman, M., and Withers, A.C. (2009) Trace element partitioning between garnet lherzolite and carbonatite at 6.6 and 8.6 GPa with applications to the geochemistry of the mantle and of mantle-derived melts. Chemical Geology, 262(1), 57–77.

Dasgupta, R., Hirschmann, M.M., and Smith, N.D. (2007) Water follows carbon: $CO_2$ incites deep silicate melting and dehydration beneath mid-ocean ridges. Geology, 35(2), 135–138.

De Ignacio, C., Munoz, M., and Sagredo, J. (2012) Carbonatites and associated nephelinites from São Vicente, Cape Verde Islands. Mineralogical Magazine, 76(2), 311–355.

Draper, D.S., and Green, T.H. (1997) P–T phase relations of silicic, alkaline, aluminous mantle–xenolith glasses under anhydrous and C–O–H fluid saturated conditions. Journal of Petrology, 38, 1187–1224.

Druken, K.A., Long, M.D., and Kincaid, C. (2011) Patterns in seismic anisotropy driven by rollback subduction beneath the High Lava Plains. Geophysical Research Letters, 38(13), 142–154.

Druken, K.A., Kincaid, C., Griffiths, R.W., Stegman, D.R., and Hart, S.R. (2014) Plume–slab interaction: The Samoa–Tonga system. Physics of the Earth and Planetary Interiors, 232, 1–14.

Elliott, T., Plank, T., Zindler, A., White, W., and Bourbon, B. (1997) Element transport from slab to volcanic front in the Mariana arc. Journal of Geophysical Research, 102, 14991–15019.

Falloon, T.J., and Green, D.H. (1989) The solidus of carbonated, fertile peridotite, Earth Planet. Sci. Lett. 94, 364-370.

Frezzotti, M.L., Selverstone, J., Sharp, Z.D., and Compagnoni, R. (2011) Carbonate dissolution during subduction revealed by diamond-bearing rocks from the Alps. Nature Geoscience, 4 (10), 703–706.

Frezzotti, M.L., and Ferrando, S. (2015) The chemical behavior of fluids released during deep subduction based on fluid inclusions. American Mineralogist, 100, 352–377.

Fulignati, P., Kamenetsky, V.S., Marianelli, P., Sbrana, A., and Mernagh, T.P. (2001) Melt inclusion record of immiscibility between silicate, hydrosaline, and carbonate melts:

94 Applications to skarn genesis at Mount Vesuvius. Geology, 29, 1043–1046.
95 Ghosh, S., Ohtani, E., Litasov, K.D., Hidenori Terasaki, H. (2009) Solidus of carbonated
96 peridotite from 10 to 20 GPa and origin of magnesiocarbonatite melt in the Earth's deep
97 mantle, Chemical Geology 262, 17–28.
98 Gorman, P.J., Kerrick, D.M., and Connolly, J.A.D. (2006) Modeling open system metamorphic
99 decarbonation of subducting slabs. Geochemistry Geophysics Geosystems, 7(4), Q04007.
100 Green, D.H., Wallace, M.E., 1988. Mantle metasomatism by ephemeral carbonatite melts.
101 Nature, 336(6198), 459–462.
102 Grove, T.L., Parman, S.W., Bowring, S.A., Price, R.C., and Baker, M.B. (2002) The role of an
103 $H_2O$-rich fluid component in the generation of primitive basaltic andesites and andesites
104 from the Mt. Shasta region, N California. Contributions to Mineralogy and Petrology,
105 142(4), 375–396.
106 Guzmics, T., Mitchell, R.H., Szabo, C., Berkesi, M., Milke, R., and Abart, R. (2011) Carbonatite
107 melt inclusions in coexisting magnetite, apatite and monticellite in Kerimasi
108 calciocarbonatite, Tanzania: melt evolution and petrogenesis. Contributions to Mineralogy
109 and Petrology, 161(2), 177–196.
110 Hack, A.C., Thompson, A.B., and Aerts, M. (2007) Phase relations involving hydrous silicate
111 melts, aqueous fluids, and minerals. Review in Mineralogy and Geochemistry, 65, 129–185.
112 Hall, P.S., and Kincaid, C. (2001) Diapiric Flow at Subduction Zones: A Recipe for Rapid
113 Transport. Science, 292(5526), 2472–2475.
114 Hammouda, T. (2003) High-pressure melting of carbonated eclogite and experimental constraints
115 on carbon recycling and storage in the mantle. Earth and Planetary Science Letters, 214(1),
116 357–368.
117 Hammouda, T., and Laporte, D. (2000) Ultrafast mantle impregnation by carbonatite melts.
118 Geology, 28(3), 283–285.
119 Harmer, R.E. (1999) The Petrogenetic Association of Carbonatite and Alkaline Magmatism:
120 Constraints from the Spitskop Complex, South Africa. Journal of Petrology, 40(4), 525–548.
121 Hermann, J., Zheng, Y.F, and Rubatto, D. (2013) Deep Fluids in Subducted Continental Crust.
122 Elements, 9, 281–287.
123 Hildner, E., Klugel, A., and Hauff, F. (2011) Magma storage and ascent during the 1995 eruption
124 of Fogo, Cape Verde Archipelago. Contributions to Mineralogy and Petrology, 162(4), 751–

772.

Hildreth, W. (1981) Gradients in silicic magma chambers: implications for lithospheric magmatism. Journal of Geophysical Research, 86, 10153–10192.

Hirahara, Y., Kimura, J.I., Senda, R., Miyazaki, T., Kawabata, H., and Takahashi, T. (2015) Geochemical variations in japan sea back‐arc basin basalts formed by high‐temperature adiabatic melting of mantle metasomatized by sediment subduction components. Geochemistry Geophysics Geosystems, 16, 1324–1347.

Hoernle, K., Tilton, G.R., Bas, M.J., Duggen, S., and Garbeschonberg, C.D. (2002) Geochemistry of oceanic carbonatites compared with continental carbonatites: mantle recycling of oceanic crustal carbonate. Contributions to Mineralogy and Petrology, 142(5), 520–542.

Hudgins, T.R., Mukasa, S.B., Simon, A.C., Moore, G., and Barifaijo, E. (2015) Melt inclusion evidence for $CO_2$-rich melts beneath the western branch of the East African Rift: implications for long-term storage of volatiles in the deep lithospheric mantle. Contributions to Mineralogy and Petrology, 169(5), 1–18.

Irving, A.J., and Wyllie, P.J. (1975) Subsolidus and melting relationships for calcite, magnesite and the join $CaCO_3$–$MgCO_3$ 36 kb. Geochimica et Cosmochimica Acta, 39(1), 35–53.

Jarrard, R.D. (2003) Subduction fluxes of water, carbon dioxide, chlorine, and potassium. Geochemistry, Geophysics, Geosystems, 4(5).

Jeffery, A.J., and Gertisser, R. (2018) Peralkaline Felsic Magmatism of the Atlantic Islands. Frontiers in Earth Science, 6, 145.

Johnston, F.K.B., Turchyn, A.V., and Edmonds, M. (2011) Decarbonation efficiency in subduction zones: implications for warm cretaceous climates. Earth and Planetary Science Letters, 303, 143–152.

Jones, A.P., Genge, M.J., and Carmody, L. (2013) Carbonate Melts and Carbonatites. Reviews in Mineralogy and Geochemistry, 75(1), 289–322.

Kelemen, P.B., and Manning, C.E. (2015) Reevaluating carbon fluxes in subduction zones, what goes down, mostly comes up. Proceedings of the National Academy of Sciences of the United States of America, 112(30).

Keller, J. and Hoefs J. (1995) Stable isotope characteristics of recent natrocarbonatite from Oldoinyo Lengai. In Carbonatite Volcanism: Oldoinyo Lengai and the Petrogenesis of

Natrocarbonatites (ed. K. Bell and J. Keller). IAVCE I, Proc. Volcanol. 4, pp. 113–123.

Kelley, K.A., Plank, T., Farr, L., Ludden, J.N., and Staudigel, H. (2005) Geochemistry of basement carbonates from ODP Site 801 in the western Pacific Ocean. doi:10.1594/PANGAEA.707921, Supplement to: Kelley et al., 2005. Subduction cycling of U, Th, and Pb. Earth and Planetary Science Letters, 234(3–4), 369–383.

Kelley, K.A., Plank, T., Grove, T.L., Stolper, E.M., Newman, S., and Hauri, E.H. (2006) Mantle melting as a function of water content beneath back‐arc basins. Journal of Geophysical Research, 111, B09208.

Kerrick, D.M., and Connolly, J.A.D. (2001) Metamorphic devolatilization of subducted marine sediments and the transport of volatiles into the Earth's mantle. Nature, 411, 293–296.

Kim, Y.K., and Lee, D.S. (1983) Petrology of alkali volcanic rocks in northern part of Ulrung Island. Mining Geology, 16, 19–336.

Kim, K.H., Tanaka, T., Nagao, K., and Jang, S.K. (1999) Nd and Sr isotopes and K-Ar ages of the Ulreungdo alkali volcanic rocks in the East Sea, South Korea. Geochemical Journal, 33, 317–341.

Kim, S.T., Coplen, T.B., and Horita, J. (2015) Normalization of stable isotope data for carbonate minerals: Implementation of IUPAC guidelines. Geochimica et Cosmochimica Acta, 158, 276-289.

Kimura, J., Gill, J.B., Kunikiyo, T., Osaka, I., Shimoshioiri, Y., Katakuse, M., and Stern, R.J. (2014) Diverse magmatic effects of subducting a hot slab in SW Japan: Results from forward modeling. Geochemistry Geophysics Geosystems, 15(3), 691–739.

Kiseeva, E.S., Yaxley, G.M., Hermann, J., Litasov, K.D., Rosenthal, A., and Kamenetsky, V.S. (2012) An Experimental Study of Carbonated Eclogite at 3.5–5.5 GPa—Implications for Silicate and Carbonate Metasomatism in the Cratonic Mantle. Journal of Petrology, 53(4), 727–759.

Kjarsgaard, B.A., and Hamilton, D.L. (1989) The genesis of carbonatites by immiscibility. Page 388–404. In Carbonatite, Edited by Keith Bell. ISBN: 0-04-445068-0.

Kjarsgaard, B.A. (1998) Phase relations of a Carbonated High-CaO Nephelinite at 0.2 and 0.5 GPa. Journal of Petrology, 11–12, 2061–2075.

Kogarko, L., Kurat, G., and Ntaflos, T. (2001) Carbonate metasomatism of the oceanic mantle beneath fernando de noronha island, brazil. Contributions to Mineralogy and Petrology,

140(5), 577–587.

Laporte, D., Lambart, S., Schiano, P., and Ottolini, L. (2014) Experimental derivation of nepheline syenite and phonolite liquids by partial melting of upper mantle peridotites. Earth and Planetary Science Letters, 319–331.

Le Bas, M.J. (2008) Fenites associated with carbonatites. Canadian Mineralogist, 46(4), 915–932.

Lee, W.J., Wyllie, P.J., and Rossman, G,R. (1994) $CO_2$-rich glass, round calcite crystals and no liquid immiscibility in the system CaO-$SiO_2$-$CO_2$ at 2.5 GPa. American Mineralogist, 79, 1135–1144.

Lee, W.J., and Wyllie, P.J. (1994) Experimental data bearing on liquid immiscibility, crystal fractionation, and the origin of calciocarbonatites and natrocarbonatites. International Geology Review, 36(9), 797–819.

Lee, W.J., and Wyllie, P.J. (1998) Petrogenesis of Carbonatite Magmas from Mantle to Crust, Constrained by the System CaO–(MgO + FeO*)–($Na_2O$ + $K_2O$)–($SiO_2$ + $Al_2O_3$ + $TiO_2$)–$CO_2$. Journal of Petrology, 39(3), 495–517.

Lee, G.H., Yoon, Y., Nam, B.H., Lim, H., Kim, Y.S., Kim, H.J., and Lee, K. (2011) Structural evolution of the southwestern margin of the Ulleung Basin, East Sea (Japan Sea) and tectonic implications. Tectonophysics, 502(3), 293–307.

Li, C.Y., Sun, S.J., Guo, X., and Zhu, H.L. (2020) Recent progresses in plate subduction and element recycling. Solid Earth Sciences, 5, 1–7.

Li, Y. (2017) Immiscible C-H-O fluids formed at subduction zone conditions. Geochemical Perspectives Letters, 3, 12–21.

Lim, C., Kim, S., and Lee, C. (2014) Geochemical fingerprint of the primary magma composition in the marine tephras originated from the Baekdusan and Ulleung volcanoes. Journal of Asian Earth Sciences, 95, 266–273.

Litasov, K.D. and Ohtani, E. (2009) Solidus and phase relations of carbonated peridotite in the system CaO–Al2O3–MgO–SiO2–Na2O–CO2 to the lower mantle depths. Phys. Earth Planet. Int. doi:10.1016/j.pepi.2009.1007.1008

Litasov, K., Shatskiy, A., Podborodnikov, I., and Arefiev, A. (2020) Phase Diagrams of Carbonate Materials at High Pressures, with Implications for Melting and Carbon Cycling in the Deep Earth. In C.E. Manning, J.F. Lin, and W.L. Mao edited: Carbon in Earth's

Interior, Geophysical Monograph 249, 137-165.

Loges, A., Schultze, D., Klugel, A., Lucassen, F. (2019) Phonolitic melt production by carbonatite Mantle metasomatism: evidence from Eger Graben xenoliths. Contributions to Mineralogy and Petrology, 174(11).

Macdonald, R., Kjarsgaard, B.A., Skilling, I.P., Davies, G.R., Hamilton, D.L., and Black, S. (1993) Liquid immiscibility between trachyte and carbonate in ash flow tufts from Kenya. Contributions to Mineralogy and Petrology, 114(2), 276–287.

Maeyamaa, D., Suzukia, N., Kazukawaa, K., Andoc, H., (2020) Residual gas in extensive stratified Miocene Izura carbonate concretions exhibiting thermogenic origin and isotopic fractionation associated with carbonate precipitation. Marine and Petroleum Geology, 119, https://doi.org/10.1016/j.marpetgeo.2020.104466

Marty, B., and Tolstikhin, I.N. (1998) $CO_2$ fluxes from mid-ocean ridges, arcs and plumes. Chemical Geology, 145, 233–248.

Mason, E., Edmonds, M., and Turchyn, A.V. (2017) Remobilization of crustal carbon may dominate volcanic arc emissions. Science, 357, 290–294.

Mibe, K., Kanzaki, M., Kawamoto, T., Matsukage, K.N., Fei, Y., and Ono, S. (2004) Determination of the second critical end point in silicate-$H_2O$ systems using high-pressure and high-temperature X-ray radiography. Geochimica et Cosmochimica Acta, 68(24), 5189–5195.

Mitchell, R.H. (2009) Peralkaline nephelinite–natrocarbonatite immiscibility and carbonatite assimilation at Oldoinyo Lengai, Tanzania. Contributions to Mineralogy and Petrology, 158(5), 589–598.

Moine, B.N., Gregoire, M., O'Reilly, S.Y., Delpech, G., Sheppard, S.M.F., Lorand, J.P., Renac, C., Giret, A., and Cottin, J.Y. (2004) Carbonatite melt in oceanic upper mantle beneath the Kerguelen Archipelago. Lithos, 75, 239–252.

Navon, O., Hutcheon, I.D., Rossman, G.R., and Wasserburg, G.J. (1988) Mantle-derived fluids in diamond microinclusions. Nature, 335, 784–789.

Neumann, E., Wulffpedersen, E., Pearson, N.J., and Spencer, E.A. (2002) Mantle Xenoliths from Tenerife (Canary Islands): Evidence for Reactions between Mantle Peridotites and Silicic Carbonatite Melts inducing Ca Metasomatism. Journal of Petrology, 43(5), 825–857.

Nielsen, T.F.D., Solovova, I.P., and Veksler, I.V. (1997) Parental melts of melilitolite and origin

of alkaline carbonatite: evidence from crystallised melt inclusions, gardiner complex. Contributions to Mineralogy and Petrology, 126(4), 331–344.

Park, M.H., Kim, J.H., and Kil, Y.W. (2007) Identification of the late Quaternary tephra layers in the Ulleung Basin of the East Sea using geochemical and statistical methods. Marine Geology, 244(1), 196–208.

Pearce, J.A., Baker, P.E., Harvey, P.K., and Luff, I.W. (1995) Geochemical Evidence for Subduction Fluxes, Mantle Melting and Fractional Crystallization Beneath the South Sandwich Island Arc. Journal of Petrology, 36(4), 1073–1109.

Pilet, S., Baker, M.B., and Stolper, E.M. (2008) Metasomatized lithosphere and the origin of alkaline lavas. Science, 320, 916–919.

Poli, S., Franzolin, E., Fumagalli, P., and Crottini, A. (2009) The transport of carbon and hydrogen in subducted oceanic crust: An experimental study to 5 GPa. Earth and Planetary Science Letters, 278, 350–360.

Price, A.A., Jackson, M.G., Blicherttoft, J., Kurz, M.D., Gill, J.B., Blusztajn, J.S., Jenner, F., Brens, R., and Arculus, R.J. (2017) Geodynamic implications for zonal and meridional isotopic patterns across the northern Lau and North Fiji Basins. Geochemistry Geophysics Geosystems, 18(3), 1013–1042.

Prokopyev, I.R., Alexander S. Borisenko, A.S., Borovikov, A.A., Pavlova, G.G. (2016) Origin of REE-rich ferrocarbonatites in southern Siberia (Russia): implications based on melt and fluid inclusions. Mineralogy and Petrology, 110, 845–859.

Pyle, J.M., and Haggerty, S.E. (1994) Silicate-carbonate liquid immiscibility in upper-mantle eclogites: Implications for natrosilicic and carbonatitic conjugate melts. Geochimica et Cosmochimica Acta, 58(14), 2997–3011.

Rass, I.T., and Plechov, P.Y. (2000) Melt inclusions in olivines from the olivine-melilitite rock of the guli massif, northwestern siberian platform. Doklady Earth Sciences, 375(3), 1399–1402.

Ray, J.S. and Ramesh, R. (2000) Rayleigh fractionation of stable isotopes from a multicomponent source, Geochimica et Cosmochimica Acta, 64, 299–306.

Ryabchikov, I.D., Orlova, G.P., Senin, V.G. and Trubkin, N.V. (1993) Partitioning of rare earth elements between phosphate-rich carbonatite melts and mantle peridotites. Mineralogy and Petrology, 49(1–2), 1–12.

Safonov, O.G., Mityaev, A.S., Yapaskurt, V.O., Georgy A., Belyanin, G.A., Elburg, M., Rajesh, H.M., Golunova, M.A., Shcherbakov, V.D., Butvina, V.G., van Reenen, D.D., and Smit, A.C. (2020) Carbonate-silicate inclusions in garnet as evidence for a carbonate-bearing source for fluids in leucocratic granitoids associated with granulites of the Southern Marginal Zone, Limpopo Complex, South Africa. Gondwana Research, 77, 147–167.

Schrauder, M., and Navon, O. (1994) Hydrous and carbonatitic mantle fluids in fibrous diamonds from Jwaneng, Botswana. Geochimica et Cosmochimica Acta, 58, 761–771.

Selverstone, J., Franz, G., Thomas, S., and Getty, S.R. (1992) Fluid variability in 2 GPa eclogites as an indicator of fluid behavior during subduction. Contributions to Mineralogy and Petrology, 112(2), 341–357.

Shatskiy, A., Arefiev, A.V., Podborodnikov, I.V., and Litasov, K.D. (2021) Effect of water on carbonate-silicate liquid immiscibility in the system KAlSi3O8-CaMgSi2O6-NaAlSi2O6-CaMg(CO3)2 at 6 GPa: Implications for diamond-forming melts, American Mineralogist, Volume 106, pages 165–173

Simonetti, A., and Bell, K., (1994) Isotopic and geochemical investigation of the Chilwa Island Carbonatite Complex, Malawi: Evidence for a depleted mantle source region, liquid immiscibility, and open-system behavior. Journal of Petrology, 35, 1597-1621.

Simonetti, A., Bell K., Viladkar, S.G. (1995) Isotopic data from the Amba Dongar Carbonatite Complex, west-central India: Evidence for an enriched mantle source. Chemical Geology (Isotope Geoscience Section) 122, 185-198.

Sliwinski, J., Bachmann, O., Ellis, B.S., Davilaharris, P., Nelson, B.K., and Dufek, J. (2015) Eruption of Shallow Crystal Cumulates during Explosive Phonolitic Eruptions on Tenerife, Canary Islands. Journal of Petrology, 56(11), 2173–2194.

Sokolov, S.V., Veksler, I.V., and Senin, V.G. (1999) Alkalis in carbonatite magmas: new evidence from melt inclusions. Petrology, 7(6), 602–609.

Spandler, C., and Pirard, C. (2013) Element recycling from subducting slabs to arc crust: a review. Lithos, 170–171, 208–223.

Staudigel, H. (2003) Hydrothermal alteration processes in the oceanic crust. In: Rudnick, R.L. (Ed.), Treatise on Geochemistry: The Crust, 511–535.

Sverjensky, D.A., Stagno, V., and Huang, F. (2014) Important role for organic carbon in subduction-zone fluids in the deep carbon cycle. Nature Geoscience, 7, 909–913.

311 Sweeney, R.J., 1994. Carbonatite melt compositions in the Earth's mantle. Earth Planet. Sci. Lett.
312 128, 259–270.
313 Tilton, G.R., and Kwon, S.T. (1990) Isotopic evidence for crust-mantle evolution with emphasis
314 on the Canadian Shield. Chemical Geology, 83(3), 149–163.
315 Troll, V.R., and Schmincke, H. (2002) Magma Mixing and Crustal Recycling Recorded in
316 Ternary Feldspar from Compositionally Zoned Peralkaline Ignimbrite 'A', Gran Canaria,
317 Canary Islands. Journal of Petrology, 43(2), 243–270.
318 Troll, V.R., Hilton, D.R., Jolis, E.M., Chadwick, J.P., Blythe, L., Deegan, F.M., and Zimmer, M.
319 (2012) Crustal $CO_2$ liberation during the 2006 eruption and earthquake events at Merapi
320 volcano, Indonesia. Geophysical Research Letters, 39(11), L11302.
321 Veksler, I.V., Dorfman, A.M., Dulski, P., Kamenetsky, V.S., Danyushevsky, L.V., Jeffries, T.,
322 and Dingwell, D.B. (2012) Partitioning of elements between silicate melt and immiscible
323 fluoride, chloride, carbonate, phosphate and sulfate melts, with implications to the origin of
324 natrocarbonatite. Geochimica et Cosmochimica Acta, 79, 20–40.
325 Wallace, M.E., and Green, D.H. (1988) An experimental determination of primary carbonatite
326 magma composition. Nature, 335(6188), 343–346.
327 Walter, M.J., Bulanova, G.P., Armstrong, L.S., Keshav, S., Blundy, J.D., Gudfinnsson, G., Lord,
328 O.T., Lennie, A.R., Clark, S.M., Smith, C.B., and Gobbo, L. (2008) Primary carbonatite
329 melt from deeply subducted oceanic crust. Nature, 454(7204), 622–625.
330 Weaver, B.L. (1991) Trace element evidence for the origin of ocean-island basalts. Geology,
331 19(2), 123–126.
332 Weidendorfer, D., Schmidt, M.W., and Mattsson, H.B. (2016) Fractional crystallization of Si-
333 undersaturated alkaline magmas leading to unmixing of carbonatites on Brava Island (Cape
334 Verde) and a general model of carbonatite genesis in alkaline magma suites. Contributions
335 to Mineralogy and Petrology, 171(5), 1–29.
336 Weiss, Y., McNeill, J., Pearson, D.G., Nowell, G.M., and Ottley, C.J. (2015) Highly saline fluids
337 from a subducting slab as the source for fluid-rich diamonds. Nature, 524, 339–342.
338 Whitley, S., Gertisser, R., Halama, R., Preece, K., Troll, V.R., Deegan, F.M. (2019) Crustal CO2
339 contribution to subduction zone degassing recorded through calc-silicate xenoliths in arc
340 lavas. Scientific Reports, 9:8803 | https://doi.org/10.1038/s41598-019-44929-2
341 Wolf, J.A. (1985) Zonation, mixing and eruption of silica-undersaturated alkaline magma: a case

342 study from Tenerife, Canary Islands. Geological Magazine, 122(6), 623–640.
343 Wood, B.J., Bryndzia, L.T., and Johnson, K.E. (1990) Mantle oxidation state and its relationship
344 to tectonic environments and fluid speciation. Science, 248, 337–345.
345 Woolley, A.R., and Church, A.A. (2005) Extrusive carbonatites: A brief review. Lithos, 85(1),
346 1–14.
347 Wyllie, P.J., Jones, A.P., and Deng, J. (1996) Rare earth elements in carbonate-rich melts from
348 mantle to crust. In: Rare Earth Minerals: Chemistry, Origin and Ore deposits. Jones AP,
349 Wall F, Williams CT (eds) Chapman and Hall, London, 77–104.
350 Xu, S., Uto, K., and Kim, Y.K. (1998) K-Ar dating of volcanic rocks from Ulreung Island,
351 Korea. Geochemical Journal, 32, 117–123.
352 Yaxley, G.M., Crawford, A.J., and Green, D.H. (1991) Evidence for carbonatite metasomatism
353 in spinel peridotite xenoliths from western Victoria, Australia. Earth and Planetary Science
354 Letters, 107(2), 305–317.
355 Yaxley, G.M., and Brey, G.P. (2004) Phase relations of carbonate-bearing eclogite assemblages
356 from 2.5 to 5.5 GPa: implications for petrogenesis of carbonatites. Contributions to
357 Mineralogy and Petrology, 146(5), 606–619.
358 Zhang, G., Chen, L., Jackson, M.G., and Hofmann, A.W. (2017) Evolution of carbonated melt to
359 alkali basalt in the South China Sea. Nature Geoscience, 10(3), 229–235.
360

**Fig. 1.** (a) Simplified geological map of the Japan sea and the location of Ulleung Island. (b) Distribution of Late Cenozoic volcanic rocks on Ulleung Island and the four drilling sites in the east (GH-1), west (GH-2), south (GH-3), and north (GH-4) of Ulleung Island (modified from Kim et al., 1999). (c) Detailed sampling depths and lithological characteristics of volcanic rocks in the GH-1, GH-2, GH-3 cores.

**Fig. 2.** Petrographic and backscatter electron (BSE) images of Ulleung Island trachyte. (a) Cross polarized light petrographic image of the mineral cluster of euhedral pseudomorphic ankerite (ank) with biotite (bio), plagioclase (pl), apatite (ap), and Fe-oxide (fe-oxd). (b) Plane polarized light petrographic image of mineral cluster of euhedral pseudomorphic ankerite with plagioclase, biotite, apatite, and Fe-oxide. Biotite cuts ankerite. (c) BSE image of mineral cluster of subhedral pseudomorphic ankerite with biotite, apatite, and Fe-oxide. Fe-oxide shows alteration. Altered pseudomorphic plagioclase is at up-right corner of the image. (d) BSE image of mineral cluster of subhedral pseudomorphic ankerite with felsilicate glass (felsic) and biotite. Abundant microcrystalline apatites exist in ankerite. (e) BSE image of mineral cluster of subhedral pseudomorphic ankerite with biotite, apatite, Fe-oxide, and vesicles. Plagioclase show alteration. (f) False-color BSE image of euhedral pseudomorphic carbonate grain is composed of euhedral Mg-rich ankerite crystals (light blue) with interstitial Fe-rich ankerite (green), euhedral to subhedral apatites (yellow and red) distribute within the ankerite. The fractures in ankerite are filled with trachyte (blue). (g) BSE image of euhedral pseudomorphic ankerite with pyroxene shape, Mg-rich and Fe-rich ankerite coexisting with silicate glass, an altered Fe-oxide in the center of the grain. (h) BSE image of spherical ankerite, Mg-rich ankerite show zoning pattern and surrounded by Fe-rich ankerite, submicron size apatite and Fe-oxides are distributing in Fe-rich ankerite.

**Fig. 3.** Petrographic and backscatter electron (BSE) images of Ulleung Island trachyte. (a) Plane polarized light petrographic image of a cluster of euhedral ankerite with biotite, apatite, and Fe-oxide. Fe-oxide contains apatite and silicate inclusions. (b) Plane polarized light petrographic image shows the euhedral pseudomorphic ankerites are included in biotite. (c) BSE image of zoned biotite contains apatite, irregular ankerite, and felsilicate inclusions. (d) BSE image of hexagonal carbonate-silicate inclusion in biotite, ankerite contains apatite and Fe-oxide crystals. (e) BSE image of hexagonal carbonate inclusion in biotite, ankerite has zoning pattern with high Mg core, vesicles exist in the center, ankerite does not have inclusions of other minerals, Fe-oxide forms along the out surface the ankerite. (f) BSE image of irregular shape inclusion in biotite, ankerite coexisting with tabular albite (ab) and anorthoclase (k-fs), Fe-oxide, and aphanitic felsilicate (felsic) glass. (g) BSE image of biotite hosted hexagonal inclusion contains a euhedral apatite surrounded by silicate glass. (h) BSE image of biotite hosted irregular shape silicate inclusion, the inclusion has a devitrified Na-K felsilicate (felsic) glass core (dark) containing apatite and Fe-oxide microcrystals, the core is surrounded by K-silicate (dark gray) glass rim. (i) BSE image of biotite hosted hexagonal inclusion with ankerite core surrounded by K-silicate glass. (j) BSE image of biotite hosted irregular inclusion with ankerite core surrounded by K-silicate (felsic) glass.

**Fig. 4.** Petrographic and backscatter electron (BSE) images of Ulleung Island trachyte. (a) BSE image of coexisting biotite and ankerite, K-silicate glass distributes along with the contact between biotite and ankerite. (2) BSE image of pseudomorphic devitrified K-silicate glass grain, which contains abundant apatite and Fe-oxide. (c) Plane polarized light petrographic image of plagioclase cluster, plagioclase is altered with ankerite grains inside plagioclase. (d) Plane polarized light petrographic image of subhedral plagioclase and pseudomorphic shape ankerite,

the core of plagioclase is replaced by sericite which is surrounded by intergrowth of albite and ankerite. (e) BSE image of pseudomorphic plagioclase, which is replaced by albite-ankerite-Fe-oxide, plagioclase relicts survived in the replacement. (f) BSE image of mineral cluster with ankerite, biotite, and plagioclase, plagioclase is replaced by intergranular albite-ankerite-apatite. Biotite contains irregular ankerite inclusions. (g) BSE image of the carbonate-rich nodule in trachyte, the nodule has a carbonate sparse shell. (h) the center of the carbonate-rich nodule contains tabular albite with interstitial ankerite, pyrite (py), monazite (mnz), rutile (rt), and apatite.

**Fig. 5.** Triangle plots of (a) carbonate phases in trachyte are mainly ankerite, with some siderite and a few calcites, carbonate phases in trachybasalt are mainly calcite and siderite. (b) biotite falls mainly in magnesio-biotite range (c) feldspar phenocryst is mainly anorthoclase, some relicts in pseudomorphic altered plagioclase grains are labradorite and bytownite. Plagioclase in trachybasalt is mainly bytownite.

**Fig. 6.** (a) – (g) Harker diagram of different types of silicate components in the trachytic rocks. (h)-(i) $FeO$-$Al_2O_3$ vs $MgO$ of carbonates included in ulvöspinel and biotite.

**Fig. 7**. (a) Plot of carbon and oxygen isotopes of the euhedral pseudomorphic phase, the carbonatite areas are from Bell and Simonetti, (2010). (b) Detailed C-O isotopes of this study.

**Fig. 8.** Evolution model of Ulleung Island volcanic rocks. Carbon flux released from the subducted oceanic slab impregnated the lower crust magma chamber and generated the pseudomorphic carbonate grains.

**Table 1** Petrological description of volcanic rocks from Ulleung Island

**Table 2** Representative silicate inclusions from different types of hosts

69 **Table 3** Representative major-element (wt.%) concentrations of the different types of carbonate
70 phases in the Ulleung Island trachyte

71 **Table 4** Carbon and oxygen isotopes of the euhedral pseudomorphic phase

Table 1 Petrological description of volcanic rocks from Ulleung Island

| Sample number | Rock type | texture | phenocryst | matrix | carbonate |
|---|---|---|---|---|---|
| **GH-3** | | | | | |
| 106.2 | Trachyandesite | Porphyritic texture | Euhedral pseudomorphic carbonate grains (~20%) | Microcrystalline | <20% well-shaped carbonate grains |
| 107.4-2 | Trachyte | Porphyritic texture | Some spherical and dumbbell shape carbonate globules (~10%) | Microcrystalline | <10% spherical and dumbbell shape carbonate globules |
| 112.6 | Trachyandesite | Porphyritic texture with large numbers of Fe-oxides | Large amounts of Fe-oxides (~20%) with carbonate melt inclusions and silicate melt inclusions | Microcrystalline albite | Fe-oxide-hosted carbonate melt inclusions |
| 114.4 | Trachyandesite | Porphyritic texture | Euhedral magniso-biotite (~10%), pseudomorphic carbonate (~10%), few amounts of apatite (~5%) | Trachytic matrix with some feldspars (~10%) | Few carbonate melt inclusions |
| 115.4 | Trachyandesite | Porphyritic texture and trachytic matrix | Euhedral to subhedral magniso-biotite (~40%) with carbonate melt inclusions and the coexisting carbonate-silicate melt inclusions, some amounts of apatite and ilmenite (~10%) | Trachytic matrix with alkali feldspar (~15%) | 50-200 μm carbonate melt inclusions, 50-100 μm coexisting carbonate-silicate melt inclusions |
| 116-1-1 | Trachyandesite | Porphyritic, trachytic matrix | Euhedral pseudomorphic carbonate (~20%), biotite (~10%), magniso-biotite with carbonate melt inclusions and silicate melt inclusions (~10%), apatite, ilmenite | Trachytic matrix with alkali feldspar (~10%) | 1-2 mm carbonate grains, 50-200 μm carbonate melt inclusions |
| 116-1-2 | Trachyandesite | Porphyritic, trachytic matrix | Similar to 116-1-1 sample | Similar to 116-1-1 sample | Similar to 116-1-1 sample |

| | | | | | |
|---|---|---|---|---|---|
| 116-2-1 | Trachyandesite | Porphyritic, trachytic matrix | Similar to 116-1-1 sample | Similar to 116-1-1 sample | Similar to 116-1-1 sample |
| UB-1 | Trachyandesite | Porphyritic, trachytic matrix | euhedral 1-2 mm pseudomorphic carbonate (~8%), sub-anhedral plagioclase (An ~60, ~5%), biotite (~5%), apatite, ilmenite | Fine grain albite, sanidine, and small amount of interstitial clay | 10% pseudomorphic carbonate, euhedral shape with shape and clear boundary |
| UB-2 | Trachyte | Fine grain | <2% sanidine (Or ~50) phenocryst, 0.2-0.5 mm | Microcrystalline fs (Or 22-58) with interstitial clay | none |
| UB-4 | Trachyte | porphyritic, trachytic matrix | Eu-subhedral 1-3 x 3-6 mm sanidine (Or ~45), includes small biotite | Microcrystalline anorthoclase (Or 25-52) | <1% irregular shape |
| UB-5 | Trachyandesite | trachytic matrix | Small corroded carbonate, eu-subhedral apatite | Microcrystalline albite (Or <5) | A few subhedral pseudomorphic calcite, Couple of thin carbonate veins (<5%) |
| UB-6 | Trachyte | trachytic matrix | <1% sanidine (Or ~50) | Microcrystalline albite and sanidine | none |
| UB-7 | Trachyandesite | porphyritic, trachytic matrix | Eu-subhedral albite (Ab 98-99), 0.2-1 mm, 3-5% | Microcrystalline anorthoclase (Or ~16) | <2% carbonate, a few thin veins |
| UB-8 | Trachyte | porphyritic, trachytic matrix | 8-10% eu-subhedral sanidine (Or ~50) and biotite | Microcrystalline sanidine (Or 25-60) plus glass | <1% carbonate in matrix |
| UB-9 | Trachyte | Fine grain | 2% 0.5-1 mm higher Ab sanidine core (Or ~50) with K-spar (Or 93-98) | Glassy matrix with fine feldspar, albite (Ab ~90) and sanidine (Or ~90) | ~3% lithic carbonate filling vesicles |
| UB-10 | Trachyte | porphyritic, trachytic matrix | 10% 0.5-3 mm, eu-subhedral sanidine (Or 41-45) and biotite | Microcrystalline sanidine (Or 40-50) plus glass | none |
| **GH-2** | | | | | |
| UB-11 | Trachyte | porphyritic, trachytic matrix | 10% eu-subhedral 1-5 mm sanidine (Or ~50) and smaller biotite | parallel microlites showing flowing bends | none |
| UB-12 | Obsidian breccia | porphyritic, breccia texture | A few plagioclase | glass | 20% vein |
| UB-13 | obsidian | porphyritic | 10% 0.5-1 mm plagioclase (An 75-85, a few An ~50) | glass | 5% rounded carbonate fills air bubbles |

| | | | | | |
|---|---|---|---|---|---|
| UB-14 | obsidian | glassy | 1-2% 0.5 mm plagioclase (An 55-58) | glass | |
| UB-15 | Trachybasalt | porphyritic trachytic matrix | Large eu-subhedral cpx and small plagioclase (An 70-85) phenocrysts, large pseudomorphic carbonate minerals with geode texture | microlites in matrix (An ~50) | 20% carbonates, pseudomorphic shape with sharp boundary, mainly siderite and calcite with colloform texture. Some pieces of irregular shape grains look like xenolith. Calcite veins cut rock. |
| UB-16 | Trachyandesite | porphyritic trachytic matrix | 15% plagioclase (An 75-88) and pyroxene | parallel microlites (An 45-60) | Carbonate in matrix, with similar crystal size and shape as feldspars, <1% small carbonate vein |
| **GH-1** | | | | | |
| UB-17 | Trachyandesite | trachytic | <1% sanidine small crystals <0.5 mm | Microcrystalline sanidine (Or 93-99) with interstitial clay | Couple of small carbonate lithics |
| UB-18 | Trachybasalt | trachytic | few | Microcrystalline anorthoclase (Ab 70-90) and sanidine (Or 93-99) with interstitial clay | 5% small pseudomorphic calcite grains in matrix, the grain is cut by feldspar |
| UB-19 | Trachybasalt | Trachytic fine grain | few | Microcrystalline anorthoclase (Ab73Or25) and albite (Ab 92) with interstitial clay | 15% anhedral calcite coexist with feldspars |
| UB-20 | Trachybasalt Similar to UB-15 | Porphyritic with pseudomorphic calcite | Pseudomorphic calcite with pyroxene shape | Massy matrix with plagioclase (An 10-60) microcrysts and calcite | 25% carbonate in rock, some pseudomorphic shape with colloform texture within the grain, matrix contains calcite coexisting with feldspars |
| UB-21 | Trachybasalt | Porphyritic with pseudomorphic calcite | Pseudomorphic calcite, amphibole, plagioclase (An ~65, and albite An4-12Ab83-91) and wormy ilmenite, some amphibole and calcite have feldspar coating | Microcrystalline albite | 20% carbonate in rock, most pseudomorphic shape with colloform texture within the grain, some calcite grains have albite coating, carbonate alteration previous magmatism |
| UB-22 | Trachyandesite | porphyritic, pilotaxitic matrix | 10% 0.5-2 mm sanidine (Or 56-90) and muscovite | Microcrystalline tabular albite (Ab 80-97) and sanidine (OR 91) parallel distributed | Few calcite in matrix |

| | | | | | |
|---|---|---|---|---|---|
| UB-23 | Trachybasalt | porphyritic, pilotaxitic matrix | 20% 1-2 mm carbonate lithics | Microcrystalline albite | 20% 1-2 mm carbonate lithics |
| UB-24 | Trachyandesite | porphyritic trachytic matrix fine grain | <5%, <0.5 mm feldspar | Microcrystalline albite and sanidine | None |
| UB-25 | Trachybasalt | porphyritic | ~50% 0.5-3 mm anhedral clinopyroxene (Wo47-49, En 38-40, Fs 11-13), plagioclase (An62-75), ilmenite and calcite lithics | Microcrystalline plagioclase (An 11-40) and sanidine (Or ~55) | 10% pseudomorphic shape and patches of calcite |
| UB-26 | Trachyandesite Similar as UB-22 | porphyritic, pilotaxitic matrix | 20% feldspar with smectite alteration, 2-3% mafic altered to chlorite | Microcrystalline tabular feldspar | 5% subhedral pseudomorphic calcite with geode texture |
| UB-40 | Trachybasalt | porphyritic | Plagioclase phenocrysts and trachytic lithics | obsidian | < 5% calcite and clay fills gas bubbles |

*106.2, 107.4-2, 112.6, 114.4, 115.4, 116-1-1, 116-1-2, 116-2-1, UB1, UB4, UB5, UB15, UB21, UB25 mineral chemistry are from EMP, others were from SEM/EDS.

*Column GH-1 is more mafic than GH-3. Based on the mineral chemistry, UB-1 in GH3 contains plagioclase phenocryst. UB-17 in GH-1, UB-11 in GH-2 is equivalent to UB-2 to UB10 in GH-3 column, phenocryst feldspar is alkali feldspar (anorthoclase-sanidine with OR ~50). UB-12 to UB-14 in GH-2 are obsidians with plagioclase phenocrysts, matching with UB-18-19 in GH1. UB-20 to UB-23 are the rocks containing large pseudomorphic colloform carbonate minerals. UB15 and 16 in GH-2 is similar to UB23-26 in GH-1 with plagioclase and pyroxene phenocrysts.

This is the peer-reviewed, final accepted version for American Mineralogist, published by the Mineralogical Society of America.
The published version is subject to change. Cite as Authors (Year) Title. American Mineralogist, in press.
DOI: https://doi.org/10.2138/am-2022-8007. http://www.minsocam.org/

Table 2 Representative mineral chemistry of the Ulleung Island trachytic rocks

| **Samples** | Magniso-biotite | | | | | | | |
|---|---|---|---|---|---|---|---|---|
| **$SiO_2$** | 36.06 | 35.89 | 35.83 | 36.24 | 35.32 | 35.23 | 35.63 | 35.71 |
| **$TiO_2$** | 8.59 | 8.82 | 9.02 | 8.70 | 8.86 | 8.69 | 9.02 | 8.53 |
| **$Al_2O_3$** | 15.48 | 15.59 | 15.72 | 15.41 | 15.57 | 15.47 | 14.31 | 14.08 |
| **$Cr_2O_3$** | 0.02 | 0 | 0 | 0 | 0 | 0.03 | 0.13 | 0.16 |
| **$FeO_T$** | 13.21 | 13.31 | 13.19 | 13.23 | 12.95 | 12.86 | 13.27 | 13.17 |
| **MnO** | 0.21 | 0.16 | 0.18 | 0.18 | 0.18 | 0.17 | 0.27 | 0.17 |
| **MgO** | 13.86 | 14.11 | 13.81 | 14.02 | 13.56 | 13.38 | 12.14 | 12.65 |
| **CaO** | 0.10 | 0.09 | 0.08 | 0.12 | 0.08 | 0.03 | 0.08 | 0.05 |
| **$Na_2O$** | 0.76 | 0.82 | 0.83 | 0.75 | 0.80 | 0.78 | 0.82 | 0.89 |
| **$K_2O$** | 8.17 | 8.23 | 8.14 | 8.37 | 8.59 | 8.58 | 9.11 | 9.11 |
| **F** | 0.21 | 0.26 | 0.32 | 0.29 | 0.50 | 0.17 | 0 | 0.23 |
| **Cl** | 0.04 | 0.04 | 0.04 | 0.04 | 0.05 | 0.04 | 0.04 | 0.03 |
| **$SO_3$** | 0.08 | 0.08 | 0.06 | 0.09 | | | 0.06 | 0.05 |
| **BaO** | 1.42 | 1.40 | 1.32 | 1.03 | | | | |
| **Total** | 98.199 | 98.894 | 98.401 | 98.462 | 96.35 | 95.42 | 94.91 | 94.71 |
| **Samples** | Albite | | Sanidine | | | Anorthoclase | | bytownite |
| **$SiO_2$** | 69.77 | 68.65 | 65.03 | 64.54 | 68.05 | 66.32 | 54.96 | 47.23 |
| **$TiO_2$** | 0 | 0.03 | 0.08 | 0.06 | 0.09 | 0.03 | 0.05 | 0.03 |
| **$Al_2O_3$** | 19.63 | 20.18 | 18.33 | 18.97 | 19.49 | 19.69 | 27.34 | 33.28 |
| **$Cr_2O_3$** | 0 | 0 | 0 | 0.03 | 0 | 0.00 | 0 | 0.04 |
| **$FeO_T$** | 0.1 | 0.14 | 0.32 | 0.51 | 0.36 | 0.12 | 0.36 | 0.54 |
| **MnO** | 0.01 | 0 | 0 | 0 | 0.04 | 0.00 | 0 | 0 |
| **MgO** | 0 | 0 | 0.06 | 0.12 | 0.05 | 0.00 | 0.03 | 0.05 |
| **CaO** | 0.17 | 0.66 | 0.05 | 0.12 | 0.61 | 0.33 | 12.07 | 16.63 |
| **$Na_2O$** | 11.1 | 10.98 | 0.46 | 0.7 | 9.97 | 6.15 | 4.91 | 1.25 |
| **$K_2O$** | 0.11 | 0.08 | 15.48 | 14.51 | 1.14 | 8.18 | 0.83 | 0.19 |
| **Total** | 100.89 | 100.72 | 99.81 | 99.56 | 99.81 | 100.89 | 100.59 | 99.27 |
| **An** | 0.88 | 3.39 | 0.26 | 0.65 | 3.22 | 1.61 | 56.31 | 87.58 |
| **Ab** | 98.43 | 96.12 | 4.07 | 6.42 | 89.63 | 50.99 | 39.07 | 11.23 |
| **Or** | 0.68 | 0.49 | 95.67 | 92.93 | 7.16 | 47.40 | 4.61 | 1.19 |

This is the peer-reviewed, final accepted version for American Mineralogist, published by the Mineralogical Society of America.
The published version is subject to change. Cite as Authors (Year) Title. American Mineralogist, in press.
DOI: https://doi.org/10.2138/am-2022-8007. http://www.minsocam.org/

| **Samples** | Apatite | | | | | | |
|---|---|---|---|---|---|---|---|
| **$SiO_2$** | 0.02 | 0.05 | 0.10 | 0.05 | 0.08 | 0.03 | 0.08 |
| **$TiO_2$** | 0.00 | 0.00 | 0.00 | 0.02 | 0.01 | 0.00 | 0.00 |
| **$Al_2O_3$** | 0.01 | 0.03 | 0.00 | 0.00 | 0.00 | 0.00 | 0.02 |
| **$Cr_2O_3$** | 0.00 | 0.00 | 0.00 | 0.00 | 0.00 | 0.00 | 0.02 |
| **$FeO_T$** | 0.29 | 0.33 | 0.33 | 0.40 | 0.26 | 0.23 | 0.20 |
| **MnO** | 0.10 | 0.07 | 0.09 | 0.09 | 0.13 | 0.11 | 0.07 |
| **MgO** | 0.20 | 0.17 | 0.19 | 0.19 | 0.18 | 0.15 | 0.16 |
| **CaO** | 53.79 | 55.57 | 55.24 | 55.29 | 55.40 | 54.59 | 55.66 |
| **$Na_2O$** | 0.06 | 0.10 | 0.06 | 0.11 | 0.06 | 0.10 | 0.12 |
| **$K_2O$** | 0.00 | 0.01 | 0.00 | 0.00 | 0.00 | 0.01 | 0.00 |
| **$P_2O_5$** | 41.37 | 41.08 | 40.53 | 41.22 | 41.59 | 41.66 | 42.35 |
| **F** | 2.18 | 2.55 | 2.72 | 3.46 | 2.62 | 2.57 | 2.22 |
| **Cl** | 0.76 | 0.75 | 0.73 | 0.81 | 0.78 | 0.66 | 0.75 |
| **$SO_3$** | 0.06 | 0.06 | 0.07 | 0.03 | 0.01 | 0.09 | 0.05 |
| **$La_2O_3$** | 0.10 | 0.13 | 0.22 | 0.18 | 0.19 | 0.18 | 0.20 |
| **$Ce_2O_3$** | 0.36 | 0.33 | 0.29 | 0.38 | 0.41 | 0.39 | 0.45 |
| **$Pr_2O_3$** | 0.02 | 0.01 | 0.03 | 0.01 | 0.01 | 0.04 | 0.12 |
| **$Nd_2O_3$** | 0.08 | 0.12 | 0.04 | 0.19 | 0.04 | 0.13 | 0.16 |
| **$Sm_2O_3$** | 0.01 | 0.01 | 0.01 | 0.01 | 0.02 | 0.01 | 0.01 |
| **Total** | 98.31 | 100.10 | 99.31 | 100.78 | 100.49 | 99.69 | 101.52 |

| **Samples** | ulvöspinel | | | altered ulvöspinel | | rutile |
|---|---|---|---|---|---|---|
| **$SiO_2$** | 1.29 | 1.32 | 1.31 | 3.07 | 3.08 | 0.61 |
| **$TiO_2$** | 15.87 | 15.92 | 15.75 | 19.88 | 22.12 | 94.61 |
| **$Al_2O_3$** | 1.68 | 1.74 | 1.58 | 1.82 | 1.91 | 0.16 |
| **$Cr_2O_3$** | 0.09 | 0.07 | 0.06 | 0.03 | 0.06 | 0.00 |
| **$FeO_T$** | 71.67 | 71.37 | 71.17 | 52.86 | 45.80 | 1.23 |
| **MnO** | 0.00 | 0.03 | 0.00 | 0.01 | 0.02 | 0.02 |
| **MgO** | 0.02 | 0.00 | 0.05 | 0.18 | 0.15 | 0.06 |
| **CaO** | 0.09 | 0.09 | 0.09 | 0.23 | 0.26 | 0.15 |
| **$Na_2O$** | 0.05 | 0.00 | 0.04 | 0.12 | 0.08 | 0.00 |

This is the peer-reviewed, final accepted version for American Mineralogist, published by the Mineralogical Society of America.
The published version is subject to change. Cite as Authors (Year) Title. American Mineralogist, in press.
DOI: https://doi.org/10.2138/am-2022-8007. http://www.minsocam.org/

| | | | | | | | |
|---|---|---|---|---|---|---|---|
| **$K_2O$** | 0.02 | 0.00 | 0.03 | | 0.01 | 0.02 | 0.19 |
| **$Nb_2O_5$** | 0.00 | 0.08 | 0.00 | | 0.08 | 0.07 | 0.55 |
| **Total** | 90.87 | 90.74 | 90.11 | | 78.52 | 73.82 | 97.60 |

| **Samples** | Fe-rich carbonate | | Mg-rich carbonate | | siderite | | |
|---|---|---|---|---|---|---|---|
| **$SiO_2$** | 0.84 | 0.13 | 0.01 | 0 | 0.17 | 0.21 | 0.76 |
| **$TiO_2$** | 0.03 | 0.00 | 0.02 | 0.08 | 0.01 | 0.04 | 3.14 |
| **$Al_2O_3$** | 0.67 | 0.13 | 0.06 | 0.02 | 0.14 | 0.13 | 0.27 |
| **$Cr_2O_3$** | 0.02 | 0.03 | 0.05 | | 0.01 | 0.01 | 0.00 |
| **$FeO_T$** | 13.74 | 11.27 | 7.96 | 10.68 | 43.95 | 43.55 | 42.29 |
| **MnO** | 1.93 | 1.51 | 1.37 | 1.53 | 0.67 | 0.40 | 0.19 |
| **MgO** | 11.02 | 12.56 | 14.13 | 14.34 | 10.84 | 11.37 | 10.83 |
| **CaO** | 28.01 | 30.08 | 29.73 | 29.13 | 1.56 | 1.30 | 2.48 |
| **$Na_2O$** | 0.02 | 0 | 0 | 0 | 0.01 | 0.03 | 0 |
| **$K_2O$** | 0.00 | 0.01 | 0.01 | 0.06 | 0.03 | 0.02 | 0.05 |
| **$La_2O_3$** | 0.00 | 0.06 | 0.06 | | 0.03 | 0 | 0.00 |
| **$Ce_2O_3$** | 0.00 | 0.03 | 0.07 | | 0.01 | 0.05 | 0.00 |
| **Total** | 56.35 | 55.80 | 53.53 | 55.92 | 56.83 | 57.49 | 60.62 |

*Detailed data are presented in Supplementary II

This is the peer-reviewed, final accepted version for American Mineralogist, published by the Mineralogical Society of America.
The published version is subject to change. Cite as Authors (Year) Title. American Mineralogist, in press.
DOI: https://doi.org/10.2138/am-2022-8007. http://www.minsocam.org/

Table 3 Representative silicate inclusions from different type of hosts

| **Samples** | Biotite-hosted silicate inclusion | | | Biotite-hosted carbonate-silicate inclusion | | | | |
|---|---|---|---|---|---|---|---|---|
| **$SiO_2$** | 59.74 | 57.41 | 58.27 | 49.22 | 50.57 | 48.93 | 51.31 | 50.52 |
| **$TiO_2$** | 0.31 | 0.19 | 0.83 | 0.17 | 0.12 | 0.17 | 0.20 | 0.24 |
| **$Al_2O_3$** | 19.86 | 21.14 | 18.77 | 30.55 | 30.82 | 31.70 | 29.21 | 29.62 |
| **$Cr_2O_3$** | 0.00 | 0.00 | 0.13 | 0.14 | 0.02 | 0.54 | 0.25 | 0.30 |
| **$FeO_T$** | 0.99 | 1.28 | 2.54 | 3.96 | 3.09 | 2.81 | 3.26 | 3.12 |
| **MnO** | 0.03 | 0.01 | 0.03 | 0.05 | 0.03 | 0.04 | 0.01 | 0.02 |
| **MgO** | 0.28 | 0.57 | 1.24 | 1.82 | 1.56 | 1.17 | 1.80 | 1.77 |
| **CaO** | 0.16 | 0.42 | 0.62 | 0.16 | 0.11 | 0.18 | 0.02 | 0.06 |
| **$Na_2O$** | 4.93 | 4.98 | 4.89 | 0.11 | 0.03 | 0.15 | 0.03 | 0.06 |
| **$K_2O$** | 7.58 | 6.51 | 5.10 | 8.859 | 9.85 | 9.58 | 9.80 | 9.85 |
| **$P_2O_5$** | 0.00 | 0.00 | | 0 | 0 | 0.00 | 0.00 | 0.00 |
| **F** | 0.00 | 0.04 | | 0.06 | 0.24 | 0.06 | 0.24 | 0.38 |
| **Cl** | 0.03 | 0.03 | | 0.01 | 0 | 0.00 | 0.00 | 0.01 |
| **$SO_3$** | 0.00 | 0.00 | | 0.03 | 0.01 | 0.01 | 0.03 | 0.00 |
| **Total** | 93.90 | 92.58 | 92.42 | 95.09 | 96.34 | 95.31 | 96.09 | 95.84 |

| **Samples** | Ulvöspinel-hosted silicate inclusion | | | Silicate in pseudomorphic carbonate grain | | Silicate grain | |
|---|---|---|---|---|---|---|---|
| **$SiO_2$** | 42.45 | 48.59 | 51.07 | 44.60 | 43.16 | 50.35 | 51.33 |
| **$TiO_2$** | 0.54 | 0.46 | 0.42 | 1.60 | 0.49 | 0.11 | 1.16 |
| **$Al_2O_3$** | 20.99 | 27.14 | 26.50 | 20.05 | 17.55 | 29.36 | 30.21 |
| **$Cr_2O_3$** | 0.34 | 0.25 | 0.13 | 0.25 | 0.36 | 0.02 | 0.03 |
| **$FeO_T$** | 10.81 | 4.73 | 3.36 | 12.84 | 16.14 | 2.84 | 2.71 |
| **MnO** | 0.11 | 0.06 | 0.03 | 0.10 | 0.02 | 0.06 | 0.04 |
| **MgO** | 6.20 | 2.38 | 1.97 | 7.35 | 10.65 | 1.39 | 1.30 |
| **CaO** | 1.31 | 0.93 | 0.89 | 1.04 | 1.01 | 0.07 | 0.14 |
| **$Na_2O$** | 0.03 | 0.03 | 0.31 | 0.02 | 0.04 | 0.12 | 0.09 |
| **$K_2O$** | 0.74 | 2.42 | 2.83 | 4.77 | 1.41 | 10.14 | 8.68 |
| **$P_2O_5$** | 0.00 | 0.00 | 0.01 | 0.01 | 0.05 | 0.02 | 0.00 |
| **F** | | | | | | 0.12 | 0.23 |

| | | | | | | | |
|---|---|---|---|---|---|---|---|
| **Cl** | | | | | | 0.03 | 0 |
| **$SO_3$** | | | | | | 0.06 | 0.06 |
| **Total** | 83.53 | 86.97 | 87.50 | 92.64 | 90.88 | 94.70 | 96.01 |

*Detailed data are presented in Supplementary II

This is the peer-reviewed, final accepted version for American Mineralogist, published by the Mineralogical Society of America.
The published version is subject to change. Cite as Authors (Year) Title. American Mineralogist, in press.
DOI: https://doi.org/10.2138/am-2022-8007. http://www.minsocam.org/

Table 4 Representative major-element (wt.%) concentrations of the different types of carbonate phases in the Ulleung Island trachytic rocks

| **Samples** | Biotite-hosted carbonate inclusion | | | Biotite-hosted carbonate-silicate inclusion | | |
|---|---|---|---|---|---|---|
| **$SiO_2$** | 0 | 0.98 | 0.24 | 0.12 | 0 | 0 |
| **$TiO_2$** | 0.01 | 0.03 | 0.09 | 0.07 | 0.05 | 0.01 |
| **$Al_2O_3$** | 0.12 | 0.85 | 0.26 | 0.2 | 0.13 | 0.03 |
| **$FeO_T$** | 9.08 | 14.33 | 11.57 | 12.29 | 8.66 | 17.19 |
| **MnO** | 0.31 | 1.01 | 0.72 | 2.24 | 0.86 | 1.49 |
| **MgO** | 14.52 | 11.49 | 11.76 | 10.8 | 12.62 | 9.14 |
| **CaO** | 30.83 | 27.83 | 27.16 | 30.75 | 32.42 | 28.2 |
| **$Na_2O$** | 0 | 0.03 | 0.01 | 0 | 0 | 0 |
| **$K_2O$** | 0.07 | 0.03 | 0.05 | 0.07 | 0.11 | 0.04 |
| **$P_2O_5$** | 0.03 | 0.06 | 0.03 | 0.02 | 0.01 | 0 |
| **SrO** | 0 | 0.06 | 0.04 | 0.06 | 0.05 | 0.03 |
| **Total** | 54.95 | 54.94 | 51.93 | 56.62 | 54.91 | 56.13 |

| **Samples** | Ulvöspinel-hosted carbonate inclusion | Fe-dominated carbonate in the rim of spherical shape carbonate globules | Mg-dominated carbonate in the core of spherical shape carbonate globules | Dumbbell shape carbonate globules | |
|---|---|---|---|---|---|
| **$SiO_2$** | 0 | 0.00 | 0.00 | 0.00 | 0.00 |
| **$TiO_2$** | 0 | 0.01 | 0.01 | 0.00 | 0.00 |
| **$Al_2O_3$** | 0.01 | 0.01 | 0.03 | 0.03 | 0.02 |
| **$FeO_T$** | 16.78 | 9.93 | 5.00 | 4.25 | 10.51 |
| **MnO** | 0.63 | 1.02 | 0.25 | 0.74 | 0.88 |
| **MgO** | 10.42 | 13.23 | 17.76 | 18.08 | 14.18 |
| **CaO** | 28.46 | 29.87 | 31.13 | 29.79 | 28.97 |
| **$Na_2O$** | 0.01 | 0.01 | 0.01 | 0.01 | 0.01 |
| **$K_2O$** | 0.01 | 0.01 | 0.01 | 0.01 | 0.00 |
| **$P_2O_5$** | 0 | 0.01 | 0.01 | 0.02 | 0.02 |
| **SrO** | 0.02 | 0.03 | 0.03 | 0.02 | 0.03 |
| **Total** | 56.34 | 54.13 | 54.24 | 52.95 | 54.62 |

| **Samples** | Mg-rich, Ca-rich, Fe-deficit carbonate in the core of pseudomorphic carbonate | | | Mg-deficit, Ca-deficit, Fe-rich carbonate in the pseudomorphic carbonate | |
|---|---|---|---|---|---|
| **$SiO_2$** | 0 | 0 | 0 | 0 | 0 |
| **$TiO_2$** | 0 | 0.00 | 0.02 | 0.02 | 0.05 |
| **$Al_2O_3$** | 0.03 | 0.03 | 0.04 | 0.08 | 0.11 |
| **$FeO_T$** | 7.44 | 7.67 | 8.11 | 13.32 | 12.49 |
| **MnO** | 0.81 | 0.77 | 0.67 | 0.45 | 0.53 |
| **MgO** | 12.76 | 12.65 | 13.06 | 10.27 | 10.66 |
| **CaO** | 31.53 | 32.51 | 31.42 | 30.16 | 30.40 |
| **$Na_2O$** | 0 | 0.02 | 0 | 0.00 | 0.00 |
| **$K_2O$** | 0.01 | 0 | 0 | 0.00 | 0.01 |
| **$P_2O_5$** | 0.01 | 0 | 0.04 | 0.02 | 0.02 |
| **F** | 0 | 0.21 | 0.06 | 0.00 | 0.04 |
| **Cl** | 0.03 | 0.01 | 0 | 0.01 | 0.01 |
| **Total** | 52.77 | 53.90 | 53.48 | 54.53 | 54.49 |

* Detailed data are presented in Supplementary II

This is the peer-reviewed, final accepted version for American Mineralogist, published by the Mineralogical Society of America.
The published version is subject to change. Cite as Authors (Year) Title. American Mineralogist, in press.
DOI: https://doi.org/10.2138/am-2022-8007. http://www.minsocam.org/

Table 5 Carbon and oxygen isotopes of the euhedral pseudomorphic phase

| Sample No. | $\delta^{13}C$ (VPDB, ‰) | $\delta^{13}C$ std dev | $\delta^{18}O$ (VPDB, ‰) | $\delta^{18}O$ std dev | $\delta^{18}O$ (SMOW, ‰)* |
|---|---|---|---|---|---|
| 116-80-1 | -3.98 | 0.016 | -18.84 | 0.038 | 11.49 |
| 116-80-2 | -5.21 | 0.015 | -21.93 | 0.04 | 8.30 |
| 116-91-1 | -5.35 | 0.021 | -22.58 | 0.033 | 7.64 |
| 116-91-2 | -5.62 | 0.016 | -23.05 | 0.061 | 7.15 |
| 116-91-4 | -5.45 | 0.017 | -23.33 | 0.032 | 6.86 |
| 116-00-1 | -5.26 | 0.023 | -25.69 | 0.069 | 4.43 |
| 116-00-2 | -5.08 | 0.023 | -23.42 | 0.077 | 6.77 |
| 116-00-3 | -5.18 | 0.016 | -24.89 | 0.034 | 5.25 |
| 116-00-4 | -4.65 | 0.022 | -21.28 | 0.021 | 8.97 |
| 116-00-5 | -5.52 | 0.015 | -20.78 | 0.022 | 9.48 |
| 116-01-1 | -5.76 | 0.01 | -22.79 | 0.026 | 7.41 |
| 116-01-2 | -5.50 | 0.024 | -21.83 | 0.034 | 8.40 |
| 116-01-3 | -4.72 | 0.014 | -21.95 | 0.029 | 8.28 |
| 116-01-4 | -5.21 | 0.026 | -22.95 | 0.043 | 7.25 |
| | | | | | |
| Standards | | | | | |
| 1. USC-1 | 2.10 | 0.02 | -2.08 | 0.03 | 28.77 |
| 2. USC-1 | 2.12 | 0.024 | -2.00 | 0.018 | 28.85 |
| 18. USC-1 | 2.08 | 0.018 | -2.22 | 0.045 | 28.62 |
| 19. USC-1 | 2.13 | 0.025 | -2.04 | 0.026 | 28.81 |

*Conversion of VPDB (Vienna Pee Dee Belemnite) to SMOW (Standard Mean Ocean Water) for $\delta^{18}O$ used the equation: $\delta^{18}O_{SMOW} = 1.03092 \times \delta^{18}O_{VPDB} + 30.92$ (Kim et al., 2015)

This is the peer-reviewed, final accepted version for American Mineralogist, published by the Mineralogical Society of America.
The published version is subject to change. Cite as Authors (Year) Title. American Mineralogist, in press.
DOI: https://doi.org/10.2138/am-2022-8007. http://www.minsocam.org/

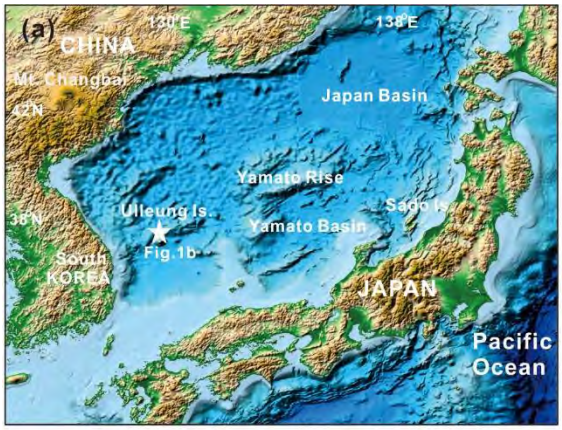


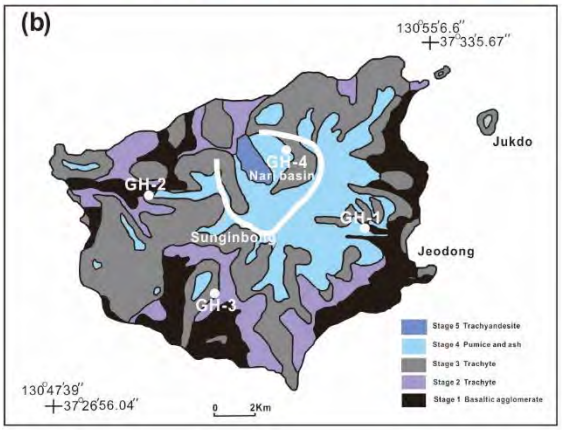


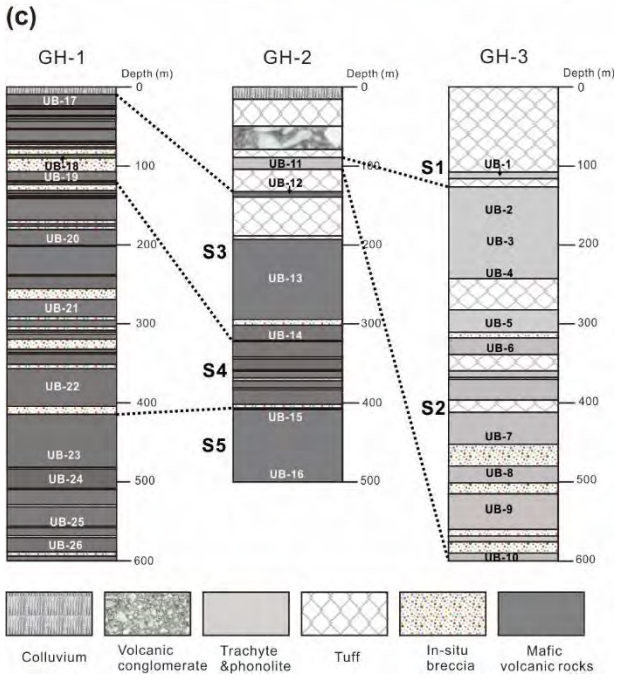


Figure 1

This is the peer-reviewed, final accepted version for American Mineralogist, published by the Mineralogical Society of America.
The published version is subject to change. Cite as Authors (Year) Title. American Mineralogist, in press.
DOI: https://doi.org/10.2138/am-2022-8007. http://www.minsocam.org/

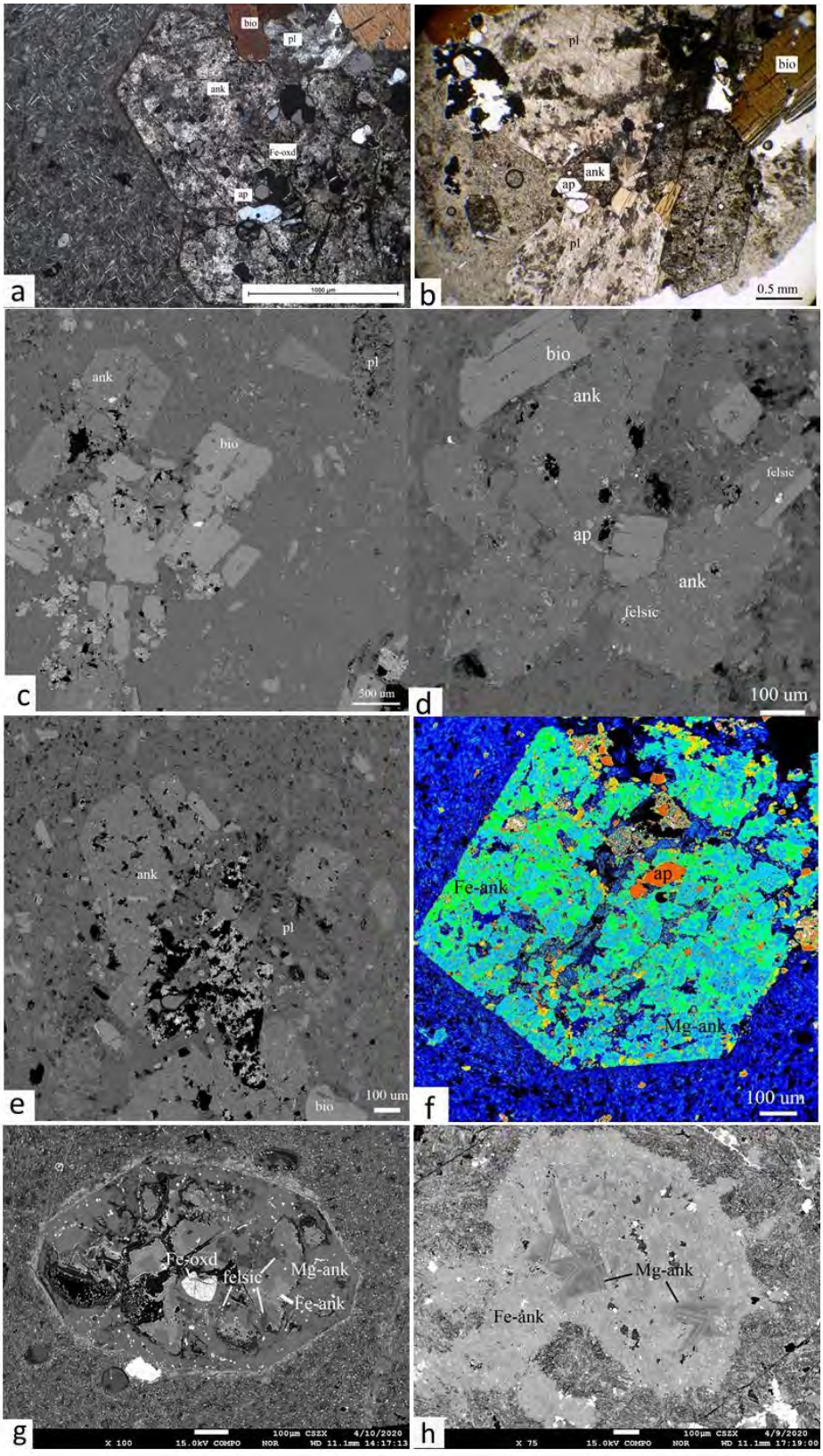


Figure 2

This is the peer-reviewed, final accepted version for American Mineralogist, published by the Mineralogical Society of America.
The published version is subject to change. Cite as Authors (Year) Title. American Mineralogist, in press.
DOI: https://doi.org/10.2138/am-2022-8007. http://www.minsocam.org/

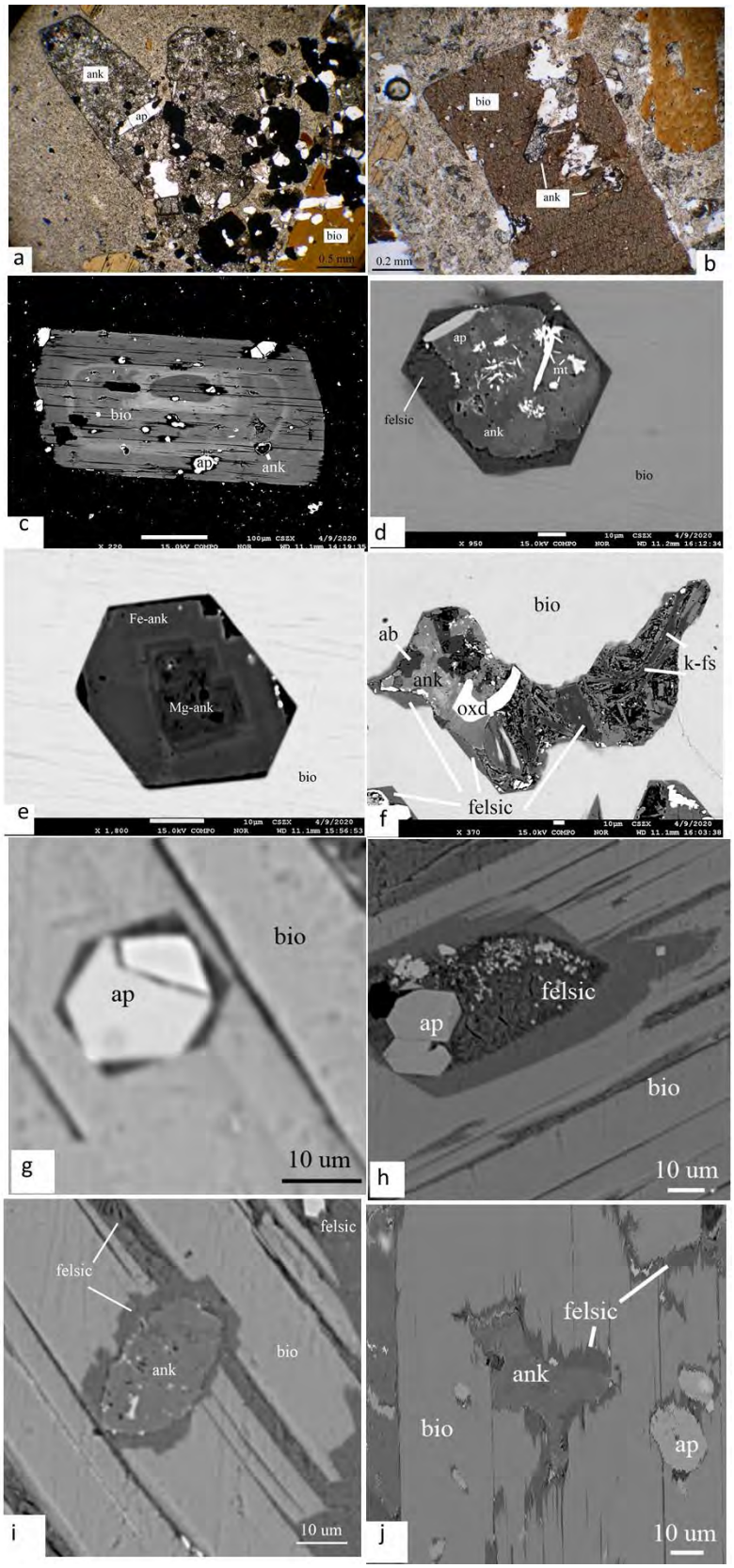


Figure 3

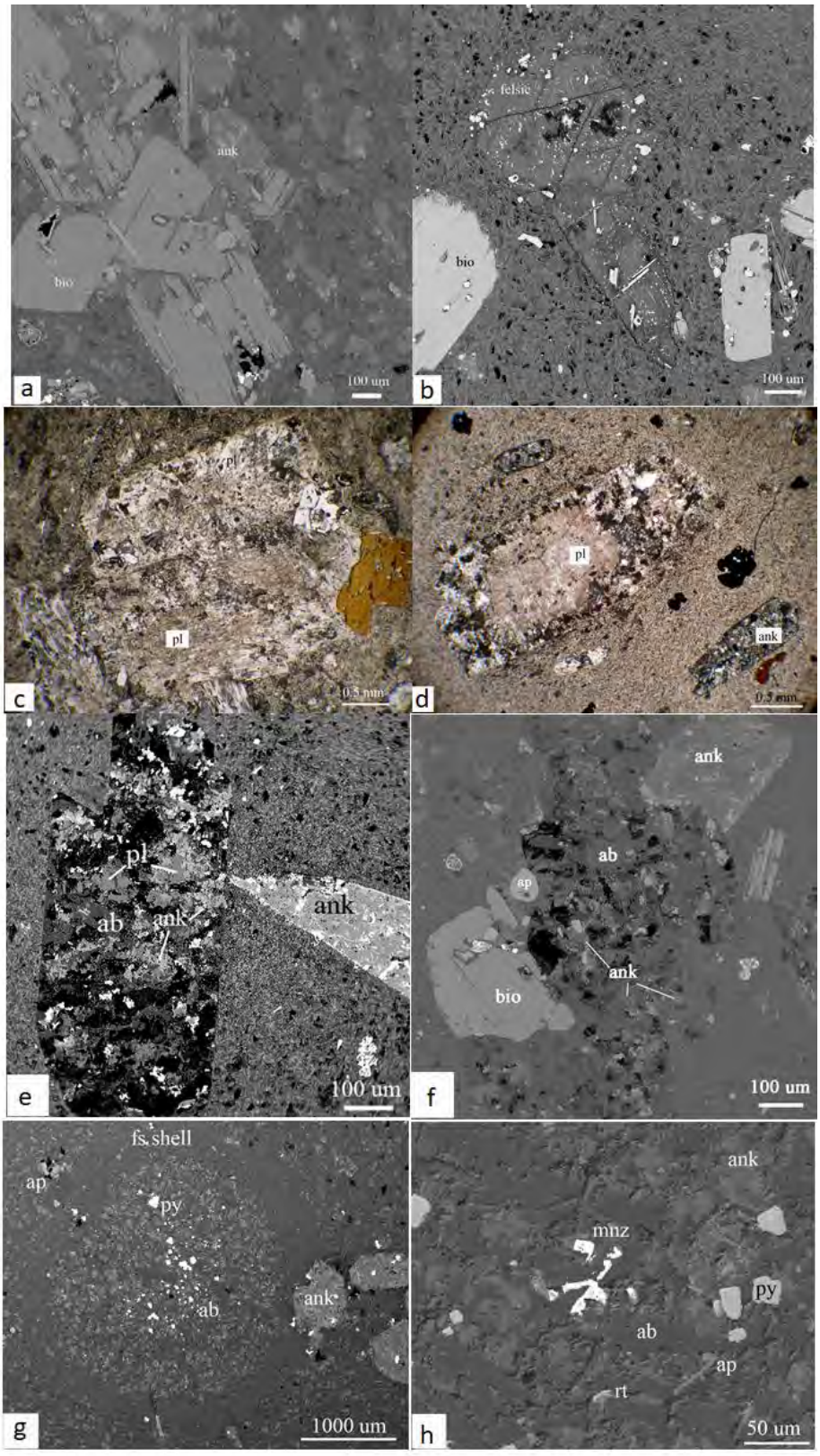


Figure 4

This is the peer-reviewed, final accepted version for American Mineralogist, published by the Mineralogical Society of America.
The published version is subject to change. Cite as Authors (Year) Title. American Mineralogist, in press.
DOI: https://doi.org/10.2138/am-2022-8007. http://www.minsocam.org/

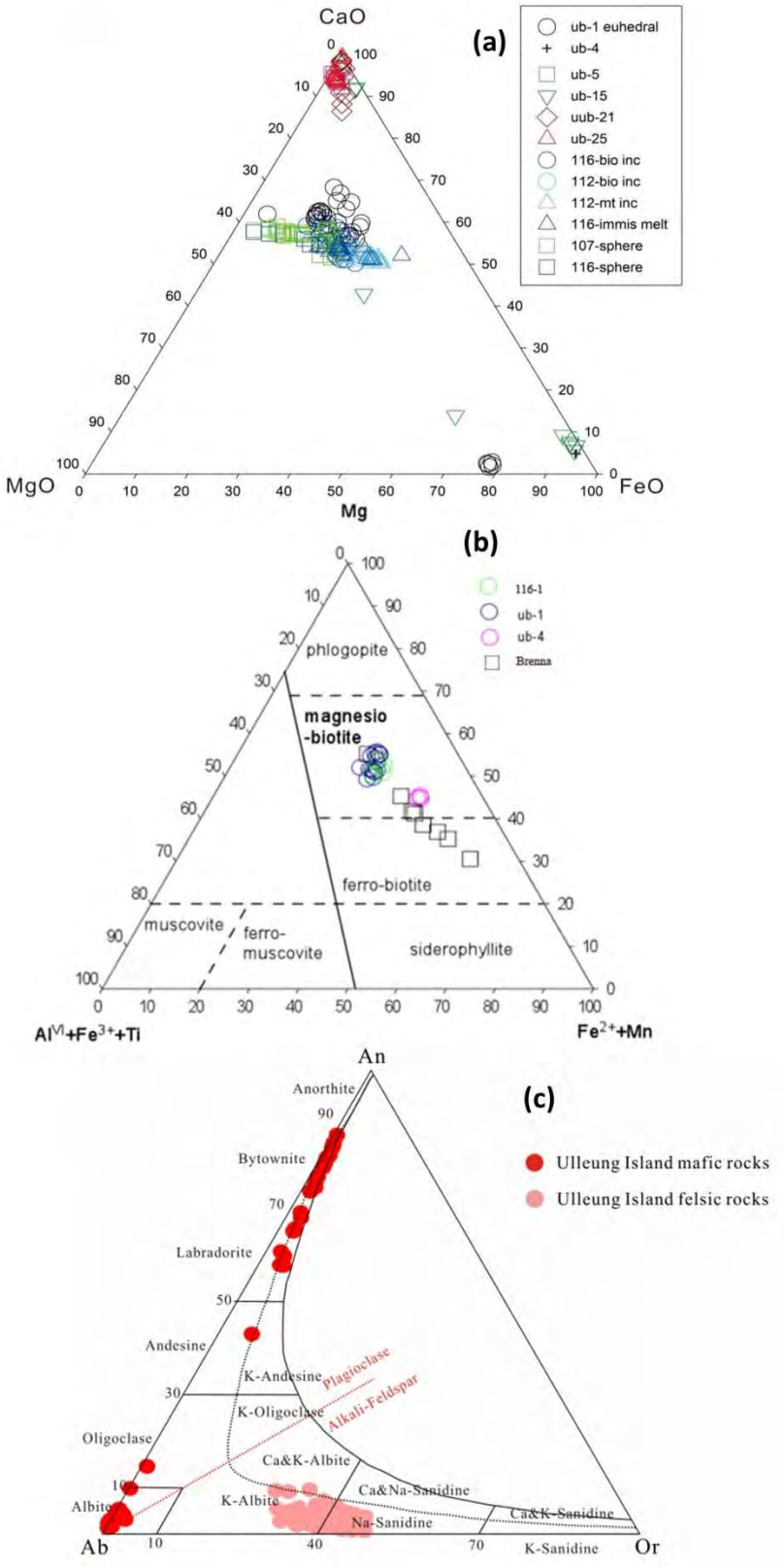


Figure 5

This is the peer-reviewed, final accepted version for American Mineralogist, published by the Mineralogical Society of America.
The published version is subject to change. Cite as Authors (Year) Title. American Mineralogist, in press.
DOI: https://doi.org/10.2138/am-2022-8007. http://www.minsocam.org/

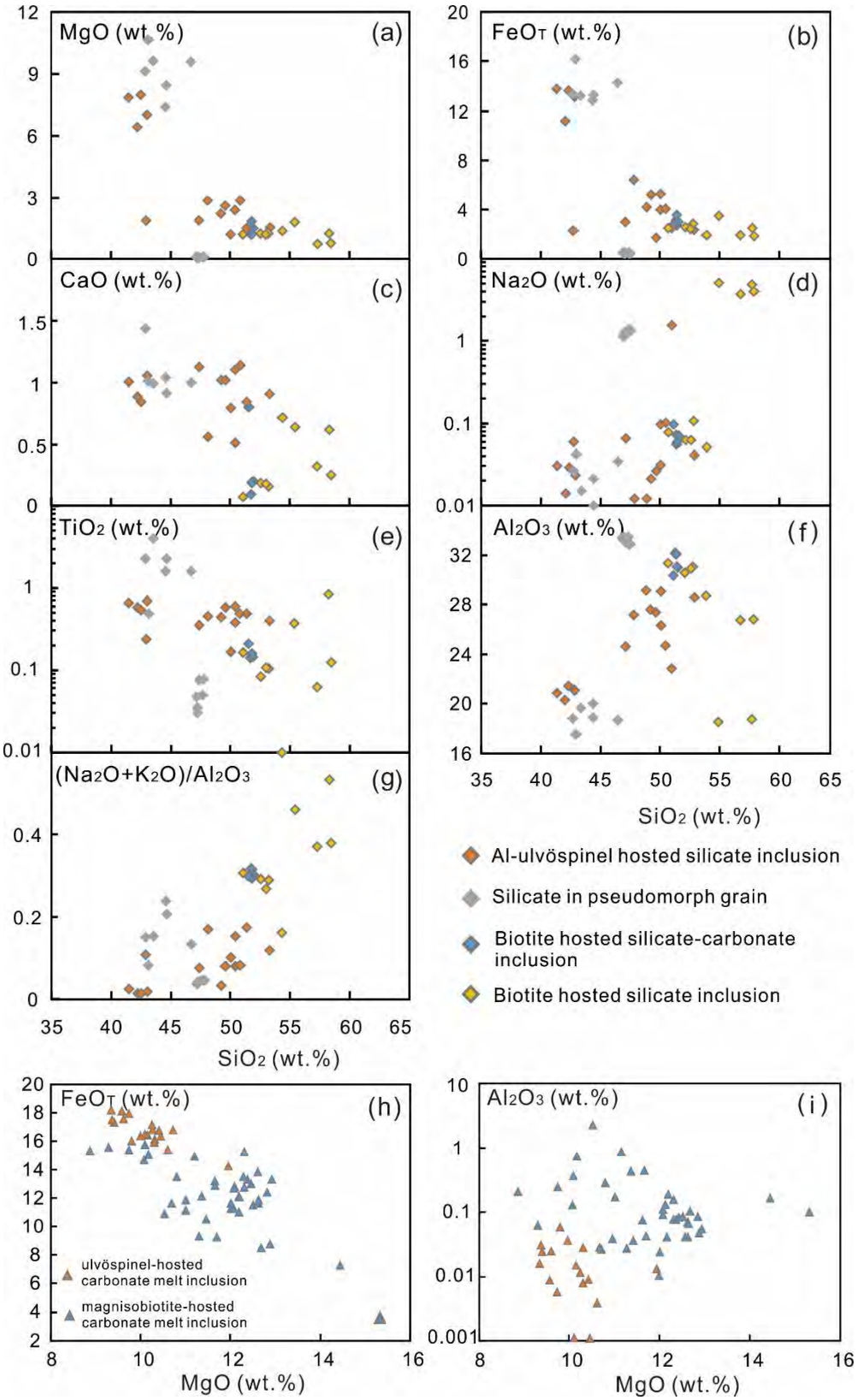


Figure 6

This is the peer-reviewed, final accepted version for American Mineralogist, published by the Mineralogical Society of America.
The published version is subject to change. Cite as Authors (Year) Title. American Mineralogist, in press.
DOI: https://doi.org/10.2138/am-2022-8007. http://www.minsocam.org/

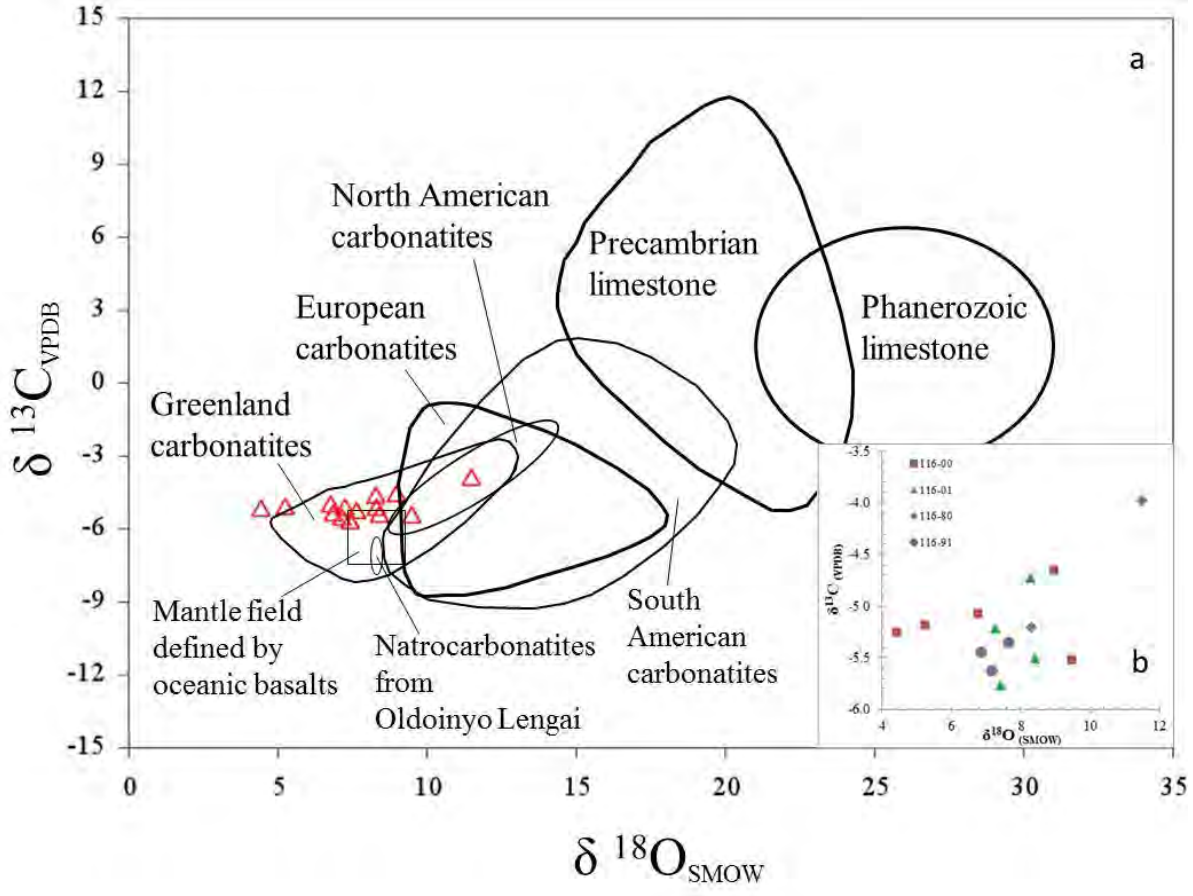


Figure 7

This is the peer-reviewed, final accepted version for American Mineralogist, published by the Mineralogical Society of America.
The published version is subject to change. Cite as Authors (Year) Title. American Mineralogist, in press.
DOI: https://doi.org/10.2138/am-2022-8007. http://www.minsocam.org/

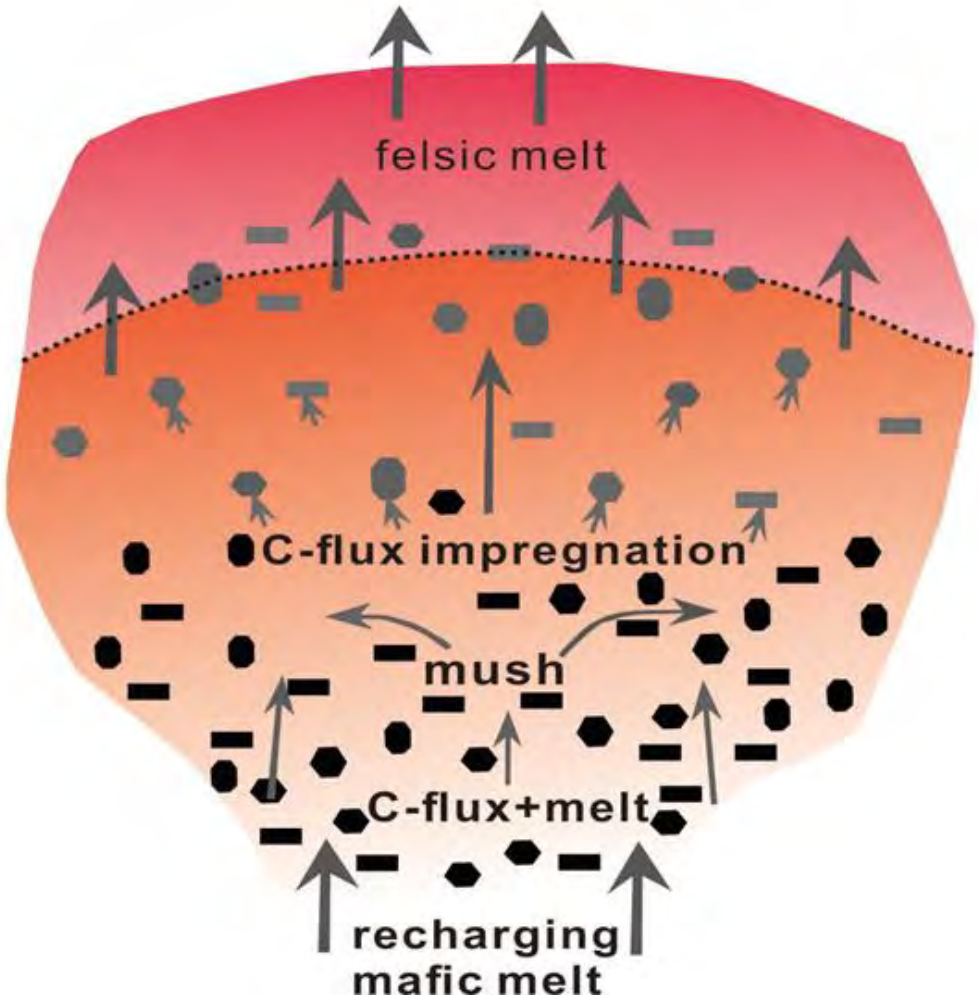


Figure 8